



University of Kentucky
UKnowledge

Theses and Dissertations--Electrical and
Computer Engineering

Electrical and Computer Engineering

2020

Nanostructured Device Designs for Enhanced Performance in CdS/Cu₂S Heterojunction Solar Cells

Benjamin Wells

University of Kentucky, brwe224@g.uky.edu

Digital Object Identifier: <https://doi.org/10.13023/etd.2020.166>

[Right click to open a feedback form in a new tab to let us know how this document benefits you.](#)

Recommended Citation

Wells, Benjamin, "Nanostructured Device Designs for Enhanced Performance in CdS/Cu₂S Heterojunction Solar Cells" (2020). *Theses and Dissertations--Electrical and Computer Engineering*. 151.
https://uknowledge.uky.edu/ece_etds/151

This Master's Thesis is brought to you for free and open access by the Electrical and Computer Engineering at UKnowledge. It has been accepted for inclusion in Theses and Dissertations--Electrical and Computer Engineering by an authorized administrator of UKnowledge. For more information, please contact UKnowledge@lsv.uky.edu.

STUDENT AGREEMENT:

I represent that my thesis or dissertation and abstract are my original work. Proper attribution has been given to all outside sources. I understand that I am solely responsible for obtaining any needed copyright permissions. I have obtained needed written permission statement(s) from the owner(s) of each third-party copyrighted matter to be included in my work, allowing electronic distribution (if such use is not permitted by the fair use doctrine) which will be submitted to UKnowledge as Additional File.

I hereby grant to The University of Kentucky and its agents the irrevocable, non-exclusive, and royalty-free license to archive and make accessible my work in whole or in part in all forms of media, now or hereafter known. I agree that the document mentioned above may be made available immediately for worldwide access unless an embargo applies.

I retain all other ownership rights to the copyright of my work. I also retain the right to use in future works (such as articles or books) all or part of my work. I understand that I am free to register the copyright to my work.

REVIEW, APPROVAL AND ACCEPTANCE

The document mentioned above has been reviewed and accepted by the student's advisor, on behalf of the advisory committee, and by the Director of Graduate Studies (DGS), on behalf of the program; we verify that this is the final, approved version of the student's thesis including all changes required by the advisory committee. The undersigned agree to abide by the statements above.

Benjamin Wells, Student

Dr. Vijay P. Singh, Major Professor

Dr. Aaron Cramer, Director of Graduate Studies

Nanostructured Device Designs for Enhanced Performance in CdS/Cu₂S
Heterojunction Solar Cells

THESIS

A thesis submitted in partial fulfillment of the
requirements for the degree of Master of Science in Electrical Engineering
in the College of Engineering at the University of Kentucky

By

Benjamin Reed Wells

Lexington, Kentucky

Director: Dr. Vijay P. Singh, Professor of Electrical and Computer Engineer

Lexington, Kentucky

2020

Copyright © Benjamin Reed Wells 2020

ABSTRACT OF THESIS

Nanostructured Device Designs for Enhanced Performance in CdS/Cu₂S Heterojunction Solar Cells

Nanostructured CdS/Cu₂S devices have been simulated using SCAPS-1D to demonstrate enhanced performance over traditional planar device structures. Two designs were examined: a nanowire CdS/planar Cu₂S device and a nanowire CdS/nanowire Cu₂S device. The addition of nanowires to a device had been previously demonstrated to improve device performance in a nanowire CdS/planar CdTe device by decreasing the amount of light absorbed by the CdS window layer, thus allowing more light to reach the absorber layer. Additionally, the total number of interface states can be greatly reduced due to the decreased total surface area between the window and absorber layers. The nanowire CdS/planar Cu₂S device showed an increase in efficiency of 0.88% over an optimized planar device. The nanowire CdS/nanowire Cu₂S device showed an increase in efficiency of 1.16% over the optimized planar device. This shows that there is a significant benefit to the addition of nanostructures to CdS/Cu₂S solar cell devices.

KEYWORDS: Solar cells, nanostructures, Copper (1) Sulfide, Cadmium Sulfide, SCAPS-1D

Benjamin Reed Wells

04/29/2020

Date

Nanostructured Device Designs for Enhanced Performance in CdS/Cu₂S
Heterojunction Solar Cells

By
Benjamin Reed Wells

Dr. Vijay P. Singh

Director of Thesis

Dr. Aaron Cramer

Director of Graduate Studies

04/29/2020

Date

ACKNOWLEDGMENTS

I am extremely grateful to everyone who has supported me during my experience studying at the University of Kentucky as a Master's student. First and foremost, I would like to thank my advisor Dr. Vijay Singh for allowing me the opportunity to join his research group and for all the guidance that he has provided during my time working with him. Without him, I would not be where I am today. I would also like to thank Dr. Todd Hasting and Dr. Aaron Cramer for taking the time to serve on my thesis committee and provide their guidance throughout the project. A special thanks must also be given to Brian Wajdyk for taking the time to train me to operate many of the pieces of equipment in CENSE as well as answering my numerous questions. I must also thank other students in Dr. Singh's group. You all have assisted me more times than I can count during my time with the group. Lastly, I thank my family for supporting me throughout the entire process that it has taken to get here.

TABLE OF CONTENTS

ACKNOWLEDGEMENTS	iii
TABLE OF CONTENTS	iv-v
LIST OF TABLES	vi
LIST OF FIGURES.....	vii-viii
CHAPTER 1: INTRODUCTION	1-7
1.1 History of Solar Cells	1-4
1.2 History of Cu ₂ S	4-6
1.3 Objective	6-7
CHAPTER 2: THEORY	8-20
2.1 Heterojunction Solar Cells	8-13
2.1.1 PN junction	8-11
2.1.2 Equivalent Circuit	11-12
2.1.3 I-V Relationship	12
2.1.4 Maximum Power Point	13
2.2 Solar Cell Parameters	13-15
2.2.1 Open Circuit Voltage	13-14
2.2.2 Short Circuit Current	14
2.2.3 Fill Factor	15
2.2.4 Efficiency	15
2.3 Cu ₂ S/CdS Heterojunction Energy Band Diagram	15-16
2.4 Bohr Radius	16-17
2.5 Shockley – Queisser Limit	17-19
2.6 Effective Resistance of Nanowire CdS/Planar Cu ₂ S Device Structure	19-20
CHAPTER 3: EXPERIMENTAL	21-31
3.1 Device Structures	21-22
3.2 Cleaning of Substrate	22
3.3 Microwave Plasma Etch	23
3.4 RF Sputtering of SnO ₂	23
3.5 Deposition of Titanium Film	23-24
3.5.1 Nanowire CdS/Planar Cu ₂ S Device	24
3.5.2 Nanowire CdS/Nanowire Cu ₂ S Device	24
3.6 Formation of Titania Nanotubes	24-27
3.7 Annealing of Titania Nanotubes	27
3.8 Electrodeposition of Cadmium Sulfide	28-29
3.9 Annealing of CdS nanowires	29
3.10 Formation of Cu ₂ S	29-30
3.11 Annealing of Cu ₂ S	30
3.12 Formation of Back Contacts	30-31

CHAPTER 4: SIMULATION	32-55
4.1 Simulating with SCAPS-1D	35-43
4.2 Theoretical Models	44-55
4.2.1 Nanowire CdS/Planar Cu ₂ S Model	44-54
4.2.2 Nanowire CdS/Nanowire Cu ₂ S Model	54-55
CHAPTER 5: RESULTS AND DISCUSSION	56-
5.1 Baseline Simulations	56-65
5.1.1 Thickness Optimization	56-61
5.1.2 Doping Optimization	61-65
5.2 Nanowire CdS/Planar Cu ₂ S Results	65-74
5.3 Nanowire CdS/Nanowire Cu ₂ S Results	74-79
CHAPTER 6: CONCLUSION	80-81
REFERENCES	82-87
VITA	88

LIST OF TABLES

Table 1.1: Benefits of Cu ₂ S Over Traditional Technologies	4
Table 4.1 Material Parameters of Left (Back) Contact	48
Table 4.2 Material Parameters of Cu ₂ S Layer	49
Table 4.3 Parameters of Defect 1 of Cu ₂ S	49
Table 4.4 Parameters of Defect 2 of Cu ₂ S	50
Table 4.5 Parameters of Cu ₂ S/CdS Interface Defect.....	50
Table 4.6 Material Parameters for CdS Layer	51
Table 4.7 Parameters of Defect 1 of CdS	51
Table 4.8 Material Parameters for SnO ₂ Layer	52
Table 4.9 Parameters of Defect 1 of SnO ₂	52
Table 4.10 Material Parameters of FTO	53
Table 4.11 Parameters of Defect 1 of FTO	53
Table 4.12 Material Parameters of Right (Front) Contact	54

LIST OF FIGURES

Figure 1.1 Illustration of Direct and Indirect Bandgaps	3
Figure 1.2: Decay of Cu ₂ S Based Solar Cells	6
Figure 2.1 A NP Homojunction	8
Figure 2.2 Energy Band Diagram of NP Heterojunction in Equilibrium	10
Figure 2.3 Solar Cell Equivalent Circuit	11
Figure 2.4 IV Relationship of a Solar Cell	12
Figure 2.5 Energy Band Diagram of Cu ₂ S/CdS Heterojunction Solar Cell	16
Figure 2.6 Increased Bandgap due to Discretization of Allowed Energy Levels	17
Figure 2.7 Absorber Material Bandgap versus Maximum Achievable Efficiency	18
Figure 2.8: Potential Paths for Generated Electrons to Take	19
Figure 3.1: NW CdS/Planar Cu ₂ S Device Structure	21
Figure 3.2: NW CdS/NW Cu ₂ S	22
Figure 3.3: Current During Anodization	25
Figure 3.4: SEM Image of 150nm Anodized Ti Sample	26
Figure 3.5: SEM Image of 4 μ m Anodized Ti Sample	26
Figure 3.6: 4 μ m Ti Sample Before Anodization	27
Figure 4.1: Difference in Solar Spectra	33
Figure 4.2: Example of Two Paths of Recombination at the Interface	35
Figure 4.3: Basic Solar Cell Structure in SCAPS	36
Figure 4.4: SCAPS Action Panel	37
Figure 4.5: SCAPS Solar Cell Definition Panel	38
Figure 4.6: SCAPS Layer Properties Panel	39
Figure 4.7: SCAPS Defect Properties Panel	40
Figure 4.8: Energy Distribution Options for Traps	41
Figure 4.9: SCAPS Interface Defect Properties Panel	41
Figure 4.10: SCAPS Contact Properties Panel	42
Figure 4.11: SCAPS I-V Simulation Output	43
Figure 4.12: Experimental Verification of Nanowire CdS Absorption Spectrum	45
Figure 4.13: Model of Absorption Coefficient for CdS Nanowire Coverage 100%-80%	46
Figure 4.14: Model of Absorption Coefficient for CdS Nanowire Coverage 75%-55%	46
Figure 4.15: Model of Absorption Coefficient for CdS Nanowire Coverage 50%-30%	47
Figure 4.16: Model of Absorption Coefficient for CdS Nanowire Coverage 25%-1%	47
Figure 4.17: Absorption Coefficient Profile of Cu ₂ S with Different Bandgaps	55
Figure 5.1: Thickness of Cu ₂ S Layer versus Conversion Efficiency	57
Figure 5.2: Thickness of Cu ₂ S Layer versus Open Circuit Voltage	58
Figure 5.3: Thickness of Cu ₂ S Layer versus Short Circuit Current Density	58
Figure 5.4: Thickness of Cu ₂ S Layer versus Fill Factor	59
Figure 5.5: Collection Probability and Generation versus Thickness	60
Figure 5.6: Open Circuit Voltage versus Acceptor Doping	61
Figure 5.7: Short Circuit Current Density versus Acceptor Doping	61
Figure 5.8: Fill Factor versus Acceptor Doping	63
Figure 5.9: Conversion Efficiency versus Acceptor Doping	64
Figure 5.10: Effect of CdS Coverage 100% - 40% and Doping on Open Circuit Voltage	65
Figure 5.11: Effect of CdS Coverage 35% - 1% and Doping on Open Circuit Voltage	66

Figure 5.12: Effect of CdS Coverage 100% - 40% and Doping on Short Circuit Current Density	68
Figure 5.13: Effect of CdS Coverage 35% - 1% and Doping on Short Circuit Current Density	69
Figure 5.14: Effect of CdS Coverage 100% - 40% and Doping on Fill Factor	71
Figure 5.15: Effect of CdS Coverage 35% - 1% and Doping on Fill Factor	71
Figure 5.16: Effect of CdS Coverage 100% - 40% and Doping on Conversion Efficiency	73
Figure 5.17: Effect of CdS Coverage 35% - 1% and Doping on Conversion Efficiency	73
Figure 5.18: Effect of E_g and Doping on Open Circuit Voltage	75
Figure 5.19: Effect of E_g and Doping on Short Circuit Current Density	76
Figure 5.20: Effect of E_g and Doping on Fill Factor	77
Figure 5.21: Effect of E_g and Doping on Conversion Efficiency	78

CHAPTER 1: INTRODUCTION

The vast majority of electricity produced in the world today is made using fossil fuels. These fuels are a non-renewable resource, meaning that they will run out one day. At the rate that they are currently being used, that day may come within a century or perhaps a bit later. Regardless of how soon this will occur, it is crucial that renewable energy sources are explored now to provide a sustainable alternative.

A prime candidate for a long-term sustainable energy source is solar power. A calculation done by the Department of Energy puts the potential of solar power at 89,300 TW [40]. This puts the amount of solar energy that strikes the Earth's surface in one day at $7.7155\text{E}+21$ J while the worldwide energy consumption in 2018 was $5.805\text{E}+20$ J [41]. Of course not all of this energy is able to be harnessed, but it shows that there is more than enough incoming solar energy to provide for all electrical needs.

A suitable type of solar panel must then be fabricated to capture a portion of this incoming energy. This paper explore the upper limit of one particular type of solar cell, a CdS/Cu₂S with embedded nanostructures.

1.1 History of Solar Cells

Light was first observed being absorbed and generating a voltage by Edmond Becquerel in 1839 when he illuminated a platinum electrode coated with silver chloride submerged in an electrolyte solution [1]. This behavior was named the photovoltaic effect and it was the first step towards modern solar cell devices. Solar technology slowly progressed until first modern silicon solar cell consisting of p-type and n-type doped regions was patented at Bell Labs in 1946 by researcher Russel Ohl. He developed

this device while he was working on silicon transistors, but it was not efficient enough for practical use at this point [2]. The device was further developed by Daryl Chapin, Calvin Fuller, and Gerald Pearson until it was publicly demonstrated in 1954 with a conversion efficiency of 6% [3]. This was the first large leap in efficiency and marked the point when solar cells became a serious point of interest for energy production. Solar cells were further developed from there, branching out into new materials and different device structures. Modern devices have reached a record 47.1% efficiency by employing multiple junctions stacked on top of each other [4].

The history of solar cells can be largely summarized in three generations. The first generation was primarily focused using silicon but other pure crystalline materials, such as gallium arsenide, were examined. This generation began with the development of monocrystalline solar cells at Bell Labs and expanded to include polycrystalline silicon due to it being much cheaper to make than monocrystalline. The driving force that allowed silicon to dominate this generation was the purity with which it could be processed compared to other semiconductors. With the recent development of silicon transistors, there was a plethora of research and development to draw from when fabricating silicon based solar cells.

The second generation of solar cells were called thin film solar cells. These were made of films ranging from a thickness of a few nanometers to tens of microns compared to first generation cells which were hundreds of microns thick. Some of the primary materials used in this generation include: cadmium telluride, copper indium gallium diselenide, and copper sulfide. These devices are able to be made so much thinner compared to silicon due to the difference in bandgap. Thin film materials have direct

bandgaps instead of indirect. A direct bandgap semiconductor is able to have an electron be directly excited from the valence band to the conduction band with energy greater than or equal to the material's bandgap energy. An indirect bandgap semiconductor requires both enough energy and a phonon to provide sufficient momentum. This is illustrated below in figure 1.1. As phonons randomly strike electrons, it is necessary to make indirect bandgap solar cells such as silicon much thicker to absorb the same amount of photons.

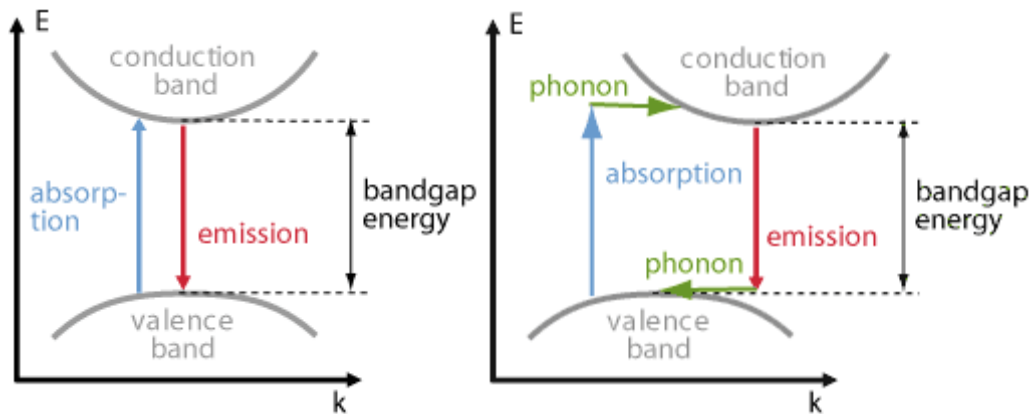


Figure 1.1 Illustration of Direct (left) and Indirect (right) Bandgaps [5]

The third and current generation of solar cells is made up of designs meant to surpass the Shockley-Queisser Limit (see section 2.5 for details on the Shockley-Queisser Limit). Researchers are trying many numerous techniques ranging from novel device structures, such as multiple junctions stacked on each other to optimally absorb different energy photons and nanostructures that take advantage of quantum effects. New materials are also being experimented with, including: perovskite solar cells, dye-sensitized solar cells, and organic solar cells. The common factor among all these

methods is that they take advantage of some mechanism not predicted by the Shockley-Quiesser Limit.

Our lab group has focused on developing third generation solar cell based on nanowire structures embedded in the window layer of the device [14, 32 - 34, 38]. This has largely been focused developing nanowire arrays for the CdS window layer in CdS/CdTe devices. Using a nanowire array for the window has several major benefit, the main one being increased transmission of photons to the absorber layer. This increase in transmission can be applied to any type of solar cell where the nanostructures can be fabrication.

1.2 History of Copper Sulfide Solar Cells

Copper (1) sulfide, Cu_2S , solar cells are part of the second generation of solar technology. Cu_2S is a highly attractive material for solar cells due to its ideal bandgap, non-toxicity, and relative price point compared to other materials. Table 1.1 compares these attributes with some common materials used for solar cells.

Table 1.1: Benefits of Cu_2S Over Traditional Technologies

Material	Cheap	Non -Toxic	Ideal Band Structure
Silicon			
CdTe			
GaAs			
Cu_2S			

CdS/Cu₂S solar cells were first developed in the 1960's and were the subject of much research due to its promising properties. A major institution that contributed to that research was the Institute of Energy Conversion at the University of Delaware, which was established by Dr. Karl Böer in 1972. Another research group, Photon Power, made strides in fabrication of CdS/Cu₂S solar cells using spray pyrolysis techniques. Efficiencies at this time were less than 5%, but this was improved up to near 10% in 1980 [36]. However, most research on Cu₂S was abandoned soon after this due to the stability of Cu₂S.

Cu₂S is known to decay relatively quickly in open air compared to other solar cells. This is due to the excessive copper diffusion within the structure. After just a few months, Cu₂S (chalcocite) can decay to Cu_{1.95}S (djurleite) which has very poor optical properties. This decay can be seen in in figure 1.2.

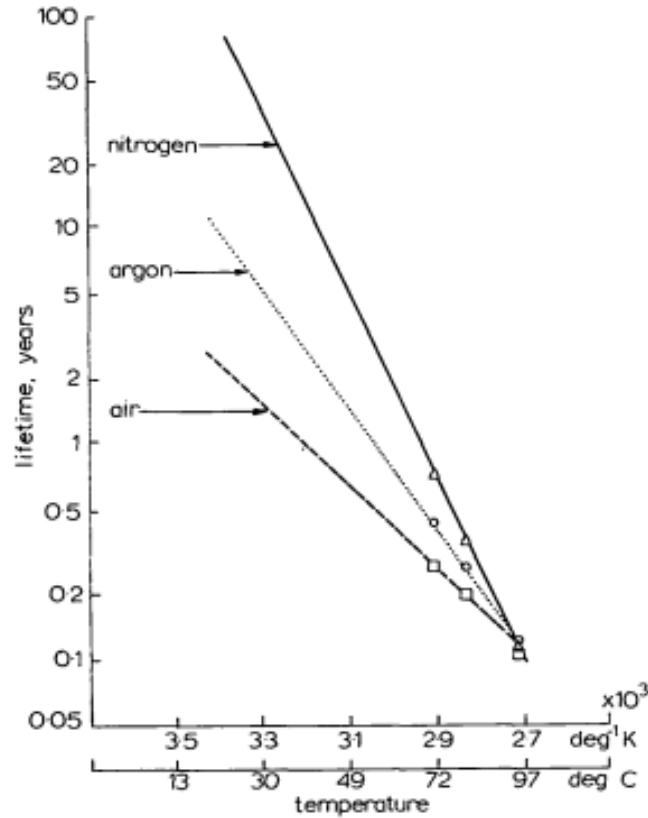


Figure 1.2: Decay of Cu₂S Based Solar Cells [42]

Some research has continued into Cu₂S over the years, but it has lost the focus of the majority of the solar cell community. Dr. Böer completed a 45 – year experimental proof in 2013 of a CdS/Cu₂S still operating after being in open air for its entire lifetime, but this experiment has not been replicated or published in a scientific journal.

1.3 Objective

The objective of this paper is simulate and determine the most efficient design for a nanostructured CdS/Cu₂S solar cell. These simulations will be carried out in three parts: 1) Simulation of planar CdS/planar Cu₂S to find the upper limits of performance without any nanostructures and establish a baseline. 2) Simulation of nanowire

CdS/planar Cu₂S to find the benefits of just using nanostructures in the window layer. 3)
Simulation of nanowire CdS/nanowire Cu₂S to find the uppermost limits possible for
CdS/Cu₂S solar cells.

This paper is broken down into six sections:

1. Introduction – A general overview of solar cells as a whole and CdS/Cu₂S as a specific type of solar cell.
2. Theory – An overview of solar cell operation, including: pn junction theory, I-V relationship, and major parameters. This section also explores the Bohr Radius and Shockley-Queisser Limit.
3. Experimental – A description of the processes required to fabricate these devices in a laboratory setting.
4. Simulation – An overview of SCAP-1D solar simulation software and the theoretical models used to simulate both device structures.
5. Results and Discussion – Analysis of the results of the simulations.
6. Conclusion – Report of final results.

CHAPTER 2: THEORY

2.1 Heterojunction Solar Cells

A typical window-absorber type p-n junction solar cell consists of three major regions, an n-type doped window layer, a p-type doped absorber layer, and a junction between them. These regions can be formed out of either the same material, as is the case in a homojunction device, or two different materials, as in a heterojunction device.

Arguably the most important region of any solar cell is the junction between the p and n regions as this is where charge separation occurs after photons are absorbed in any region of the device and thus plays a large role in determining device performance.

2.1.1 PN Junction

A pn junction is formed when two semiconductors of different doping types are brought together. Once together, the majority carriers on either side of the junction diffuse across the junction to give rise to a depletion region of width W and having a built in potential of V_{bi} .

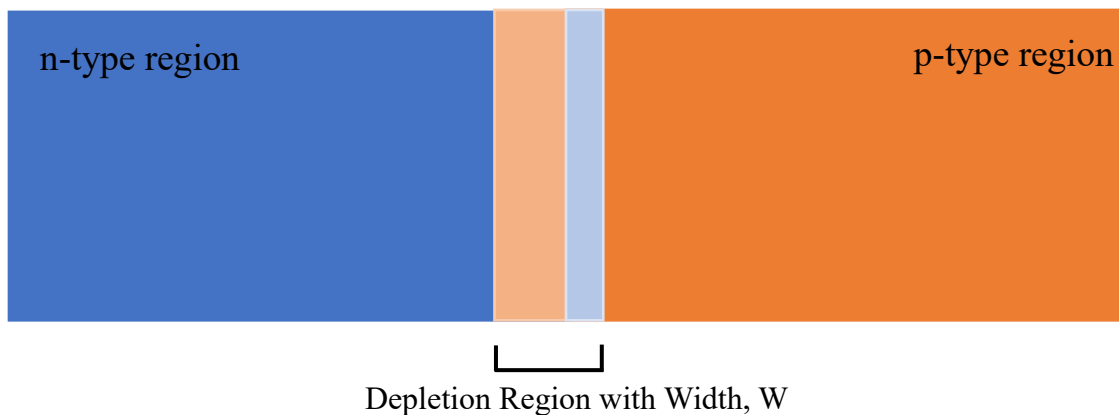


Figure 2.1 A NP Homojunction

The built-in potential and depletion width in a pn homojunction can be determined by the equations:

$$V_{bi} = \frac{kT}{q} \ln \left(\frac{N_A N_D}{n_i^2} \right) \quad [2.1]$$

$$W = \left(\frac{2V_{bi}\epsilon_s}{q} \left(\frac{1}{N_A} + \frac{1}{N_D} \right) \right)^{1/2} \quad [2.2]$$

N_A and N_D represent the doping concentration for acceptor and donors in the p-type and n-type regions while n_i is the intrinsic carrier concentration for the material. It is the built in potential across the depletion region that results in the electric field necessary to separate electrons and holes after they have been generated by an absorbed photon.

A pn heterojunction differs from the homojunction in several key ways. The first being that it consists of two materials with different material properties being brought together. It is the difference in these properties that will determine the quality of the junction, namely: the mismatch between the electron affinities, the lattice constants, and the thermal expansion coefficients. The magnitude of these mismatches will play a role in determining the magnitude of recombination centers along the junction when the device is formed.

The heterojunction structure offers several benefits over a traditional homojunction. The n-type window material can be chosen such that its bandgap is high enough to let most high energy photons pass through to be absorbed by the p-type absorption region and better contribute to the photocurrent. This region can also be highly doped to reduce the series resistance without severely affecting its transmittivity.

The built in potential for a pn heterojunction can be determined by the equation:

$$V_{bi} = E_{g2} - (E_f - E_{c2}) + \chi_2 - \chi_1 - (E_{c1} - E_f) \quad [2.3]$$

E_g , E_f , E_c , and χ represent the bandgap, fermi level, conduction band level, and electron affinities for each material in the heterojunction. The energy band diagram for a pn heterojunction can be seen in Figure 2.2.

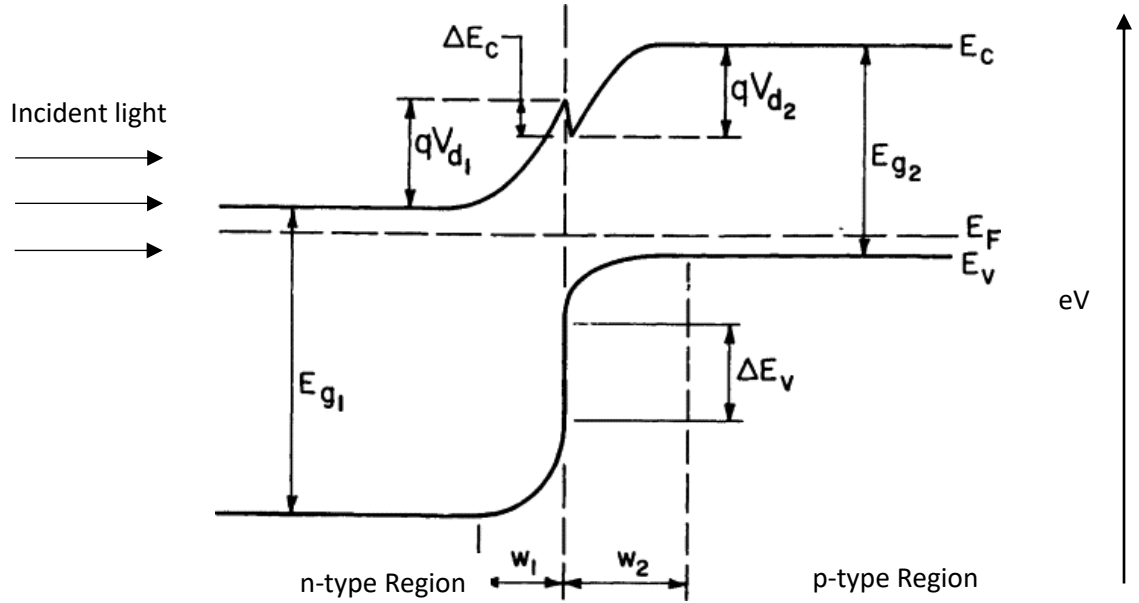


Figure 2.2 Energy Band Diagram of NP Heterojunction in Equilibrium [5]

ΔE_c and ΔE_v are the conduction and valence band discontinuities. In an ideal case, ΔE_c would depend solely on the difference in electron affinities, but it varies slightly due to differences in the lattice structure of each material. ΔE_v can be determined as the difference between ΔE_g and ΔE_c . qV_{d1} and qV_{d2} are a different notation for the built in potentials in both regions that arises from the doping.

All three regions in both the homojunction and heterojunction devices contribute to the generated photocurrent. As a photon passed through the device, if it has energy

greater than E_{g1} it will be absorbed in the n-type region and generate a hole. A photon with energy less than E_{g1} but greater than E_{g2} will be absorbed in the p-type region and generate an electron. A photon can also be absorbed in the depletion region where they form electron-hole pairs that are separated by the electric field present in that region. Recombination can occur if the electron or hole must travel further than its diffusion length or if it encounters a trap level within the device.

2.1.2 Equivalent Circuit

A solar cell can be modeled with the equivalent circuit seen below in figure 2.3.

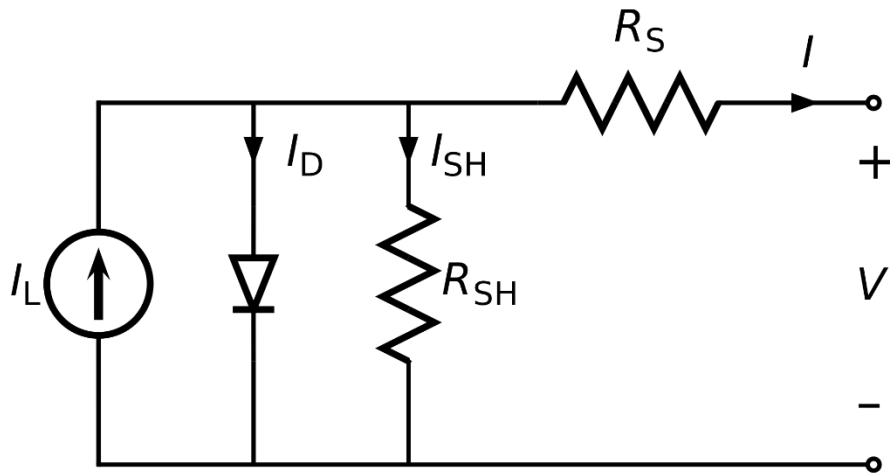


Figure 2.3: Solar Cell Equivalent Circuit [6]

In this circuit, I_L is the light generated current, I_D is the diode current, I_{SH} is the shunt current, R_{SH} is the shunt resistance, R_S is the series resistance, I is the output current and V is the voltage across the device. R_{SH} is a result of defects during the fabrication process that allows some current to take shunting paths through the device as opposed to flowing out of the device. In an ideal device, R_{SH} would be infinite. R_S is a result of the materials themselves as well as the contacts used and the overall quality of

fabrication. Ideally, R_s would be as low as possible to prevent resistive losses. The total current in the device can be written as:

$$I = I_L - I_D - I_{SH} = I_L - I_0 \left(\exp \left(\frac{V + IR_s}{nkT} \right) - 1 \right) - \frac{V + IR_s}{R_{SH}} \quad [2.4]$$

2.1.3 I-V Relationship

The IV relationship of a solar cell can be seen in the following image 2.4.

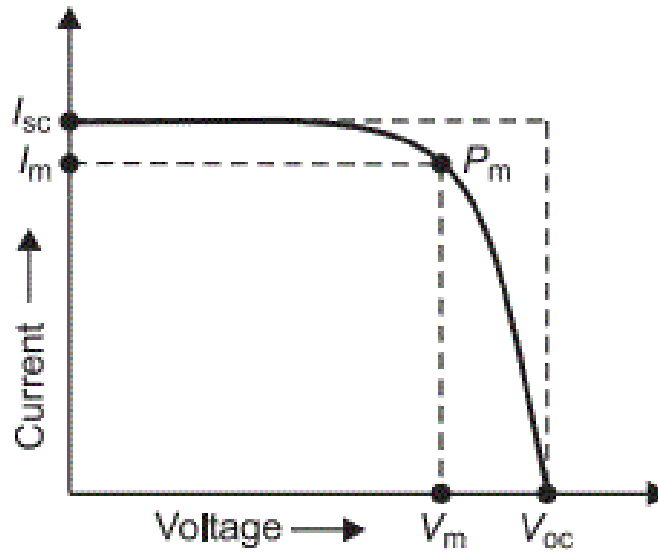


Figure 2.4: IV Relationship of a Solar Cell [7]

I_{sc} represents the short circuit current, V_{oc} is the open circuit voltage, I_m is the current at the maximum power point (MPP), and V_m is the voltage at the MPP. As can be seen above, there is a range of points to operate at, but it is most ideal to operate at the maximum power point, P_m .

2.1.4 Maximum Power Point

The power delivered by the solar cell is:

$$P = IV = \left(\frac{nkT}{q}\right) I \ln\left(\frac{I_L}{I_0}\right) [2.5]$$

To get maximum power, the device must operate at both I_m and V_m which are described by the below equations:

$$I_{mp} = I_0 \frac{qV_m}{kt} \exp\left(\frac{qV_m}{nkT}\right) \cong I_L \left(1 - \frac{nkT}{qV_{mp}}\right) [2.6]$$

$$V_{mp} = \frac{nkT}{q} \ln\left(\frac{\frac{I_L}{I_0} + 1}{1 + \frac{qV_{mp}}{nkT}}\right) \cong V_{oc} - \frac{nkT}{q} \ln\left(1 + \frac{qV_{mp}}{nkT}\right) [2.7]$$

Due to the transcendental nature of the equation for V_m , it must be found using an iterative method. Once V_m is found, then I_m can be calculated as well. Using both of the values it is now possible to find the MPP:

$$P_m = I_{mp}V_{mp} = I_{sc}V_{oc}FF \cong I_L \left(V_{oc} - \frac{q}{nkT} \ln\left(1 + \frac{qV_{mp}}{nkT}\right) - \frac{nkT}{q}\right) [2.8]$$

2.2 Solar Cell Parameters

Solar cell performance is characterized by several different factors, namely the open circuit voltage (V_{oc}), the short circuit current (I_{sc}), and the fill factor (FF). These three values give the maximum power when multiplied together as seen in equation 2.8.

2.2.1 Open Circuit Voltage

The open circuit voltage, V_{oc} , represents the output voltage with no load attached to it and is given by:

$$V_{oc} = \frac{nkT}{q} \ln \left(\frac{J_{sc}}{J_0} + 1 \right) \quad [2.9]$$

J_{sc} and J_0 are the short circuit current density and the saturation current density respectively. The saturation current density can be described as:

$$J_0 = qN_C N_V \left(\frac{1}{N_A} \sqrt{\frac{D_n}{\tau_n}} + \frac{1}{N_D} \sqrt{\frac{D_p}{\tau_p}} \right) \exp \left(\frac{-E_g}{kT} \right) \quad [2.10]$$

N_C represents the density of states in the conduction band, N_D is the density of states in the valence band, N_A is the acceptor density, N_D is the donor density, D_n is the diffusion length of electron, D_p is the diffusion length of holes, τ_n is the carrier lifetime of electrons, τ_p is the carrier lifetime of holes, and E_g is the bandgap of the absorber material.

2.2.2 Short Circuit Current

The short circuit current, I_{sc} , represents the current with zero applied bias. In the ideal case, I_{sc} is equal to I_L but due to the effects of R_s and R_{SH} there is a slight difference. I_{sc} is also typically expressed as a current density, J_{sc} and be determined by summing the current density of electrons (J_n), holes (J_p), and the photocurrent density in the space charge region (J_d) over the solar spectrum:

$$J_{sc} = \int_{\lambda_{min}}^{\lambda_{max}} (J_n + J_p + J_d) d\lambda \quad [2.11]$$

With λ_{min} representing the lower end of the solar spectrum, 300nm for our sun, and λ_{max} representing the absorption edge of the absorber material.

2.2.3 Fill Factor

The fill factor, FF, represents how ideal the solar cell is and describes how rectangular the IV curve is. A FF of 100% would result in a perfectly rectangular IV curve. It can be determined as a ratio of the maximum power to the product of V_{oc} and I_{sc} :

$$FF = \frac{V_{mp}I_{mp}}{V_{oc}I_{sc}} \quad [2.12]$$

2.2.4 Efficiency

The efficiency, η , of a solar cell is the ratio of maximum power that the cell can provide to the incoming solar power:

$$\eta = \frac{P_{MPP}}{P_{solar}} = \frac{FF * I_{sc} * V_{oc}}{P_{solar}} \quad [2.13]$$

P_{solar} can be determined by:

$$P_{solar} = A \int_0^{\infty} F(\lambda) \frac{hc}{\lambda} d\lambda \quad [2.14]$$

Where A is the device area, $F(\lambda)$ is the incident photon flux, and (hc/λ) is the energy of each incoming photon. P_{solar} can also be determined by multiplying the area of the device by 1000 W/m^2 , the average power density of sunlight at sea level.

2.3 Cu₂S/CdS Heterojunction Energy Band Diagram

Below in figure 2.5 the energy band diagram for a Cu₂S/CdS heterojunction is shown.

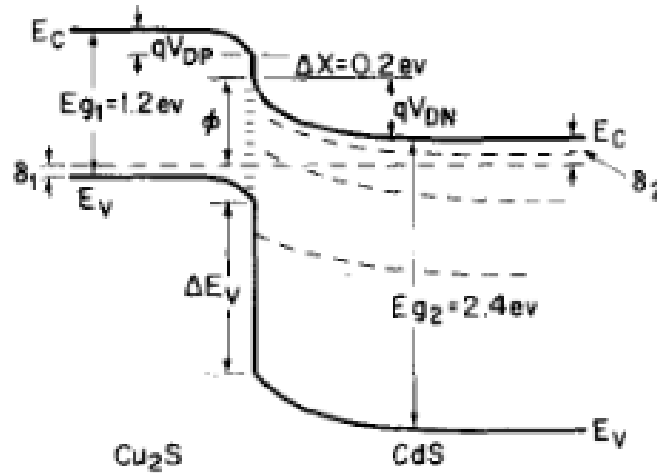


Figure 2.5 Energy Band Diagram of Cu₂S/CdS Heterojunction Solar Cell [8]

Under AM1.5 illumination, most of the light passes through the n-type CdS window layer due to its much higher bandgap; later it is absorbed by the p-type Cu₂S absorber layer.

2.4 Bohr Radius

The bandgap is typically a fixed parameter in a solar cell once a material has been chosen, but it has been shown that if the material can be formed into nanocrystals of a diameter lower than the Bohr radius, then the bandgap can be increased [9]. This is achieved by limiting the total crystal size. When the crystal size is sufficiently constrained, then the available energy levels change as well. They collapse from a near continuous curve to discrete energy levels as seen below in figure 2.6:

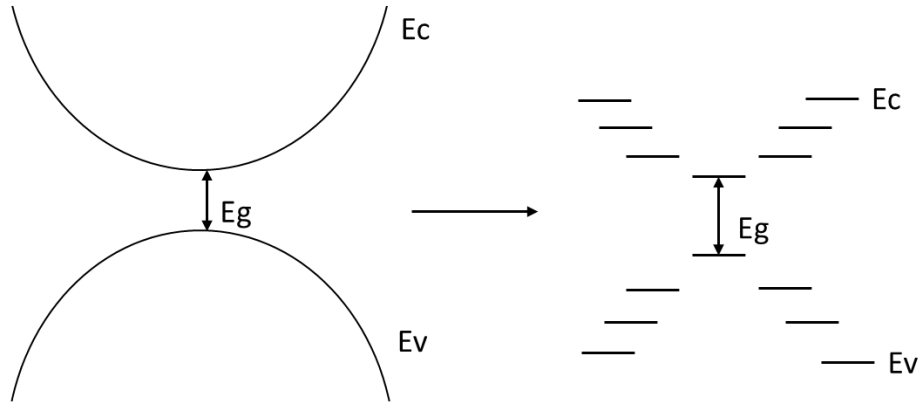


Figure 2.6: Increased Bandgap due to Discretization of Allowed Energy Levels

By taking advantage of this property it is possible to adjust the bandgap of Cu_2S to a more optimal level using the following equation developed for Cu_xS quantum dots, which were found to have a exciton Bohr radius of 3-5nm [10]:

$$E_{g(QD)} = E_{g(bulk)} + \frac{h^2}{2R^2} \left(\frac{1}{m_e} + \frac{1}{m_h} \right) \quad [2.15]$$

Where $E_{g(QD)}$ represents the effective bandgap of the quantum dot, $E_{g(bulk)}$ is the bandgap of Cu_xS , h is Planck's constant, R is the radius of the nanoparticle, m_e is the effective mass of electrons, and m_h is the effective mass of holes [10]. Using this equation, it is possible to see that decreasing the radius beyond the Bohr radius will increase the effective bandgap of the quantum dot. This can then be used to optimize the bandgap of Cu_2S by placing it into sufficiently small nanostructures.

2.5 Shockley – Queisser Limit

In 1961, William Shockley and Hans-Joachim Queisser published a paper examining the upward bound of single junction solar cell efficiency based on the

bandgap of the absorber material under a 6000K blackbody spectrum [11]. They plotted the bandgaps, V_g , versus maximum achievable efficiency, η , as seen below in figure 2.7.

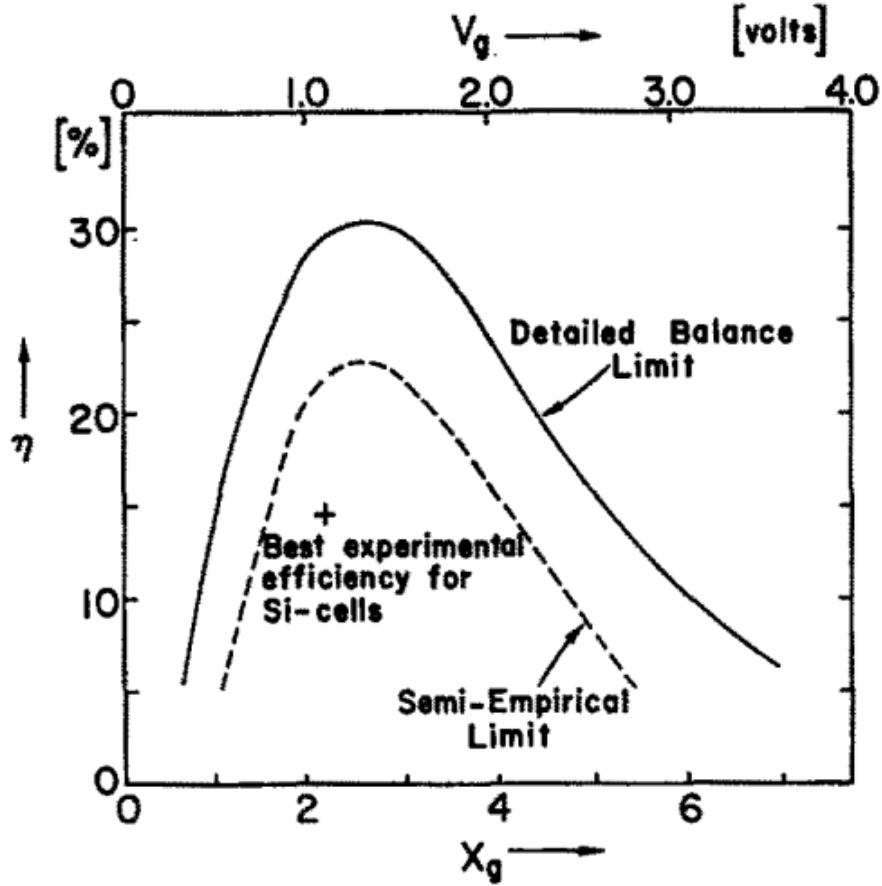


Figure 2.7: Absorber Material Bandgap versus Maximum Achievable Efficiency [11]

These values were originally calculated by taking into account bandgap, radiative recombination, and a factor the authors call t_s which they defined as: “the probability that a photon with $h\nu > E_g$ incident on the surface will produce a hole-electron pair”[11]. To reach the upper limit, this value must be as close to 1 as possible. Using all these values, they compute the theoretical maximum efficiency to occur using an absorber with E_g of approximately 1.5 eV.

This limit has been re-calculated many time taking into account the AM1.5 spectrum instead of a blackbody spectrum, other types of recombination, and many other factors. A calculation in 2016 found the limit for a single junction solar cell to be 33.7% efficient with a bandgap of 1.34 eV [13].

By fabricating Cu_2S nanostructure of an appropriate radius below the Bohr radius, it is possible to shift the bandgap to its most optimal point.

2.6 Effective Resistance of Nanowire CdS/Planer Cu_2S Device Structure

Due to the nature of the NW CdS/planar Cu_2S device, not all electrons will be generated directly above the CdS/ Cu_2S junction. This means that they will have to travel additional distance and thus encounter additional resistance when compared to a fully planar device. This is illustrated in figure 2.8.

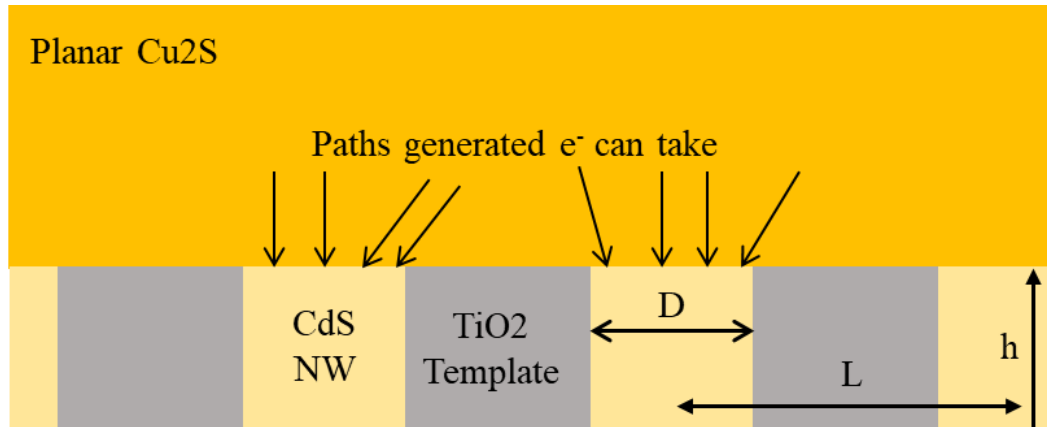


Figure 2.8: Potential Paths for Generated Electrons to Take

This process was model by Deepak Kumar in his thesis “Investigation of Host Nanotube Parameter for Enhancing Performance of Nanostructured CdS-CdTe Solar Cells” [14]. The effective resistance of a nanowire layer was found to be dependent on

the height of the nanowires, h , the width of the nanowires, D , and the interpore distance, L :

$$R_{nanowire} = R_{planar} * \left(1 + \left(\frac{L}{\sqrt{2}} - \frac{D}{2}\right) * \frac{1}{h}\right) \quad [2.16]$$

CHAPTER 3: EXPERIMENTAL

3.1 Device Structures

The experimental work done to fabricate two difference device structures will be described in this chapter. The first structure is a structure of soda lime glass/FTO/SnO₂/CdS nanowires embedded in a porous TiO₂ template/planar Cu₂S/Cu/Cr with the copper and chromium acting as both back contacts and a reflective surface. A section of the FTO that extends beyond the rest of the layers acts as the front contact. This device can be seen in figure 3.1. The second device structure uses the same materials as the first, but the porous TiO₂ template is extended to contain both the CdS and the Cu₂S. This device can be seen in figure 3.2.

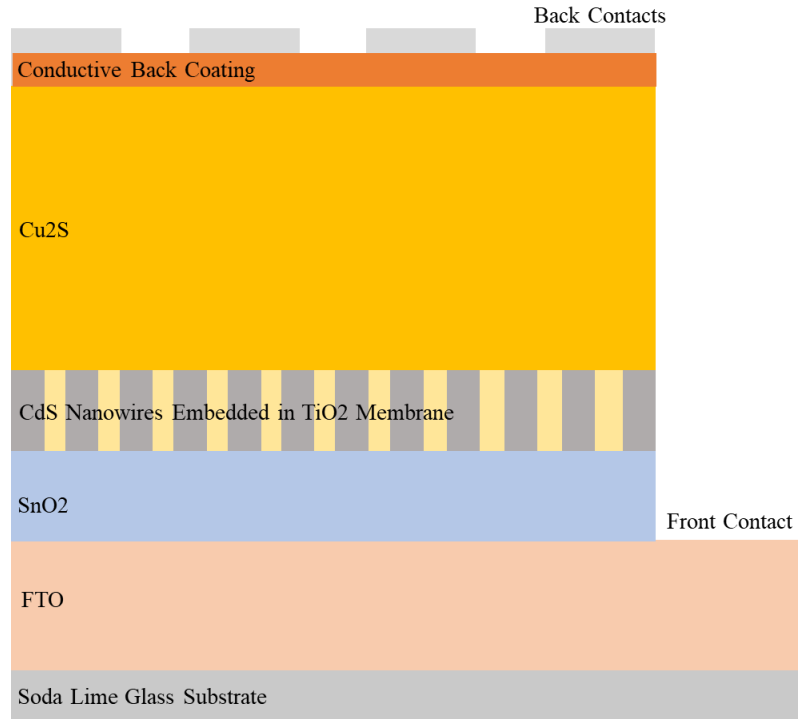


Figure 3.1: NW CdS/Planar Cu₂S Device Structure

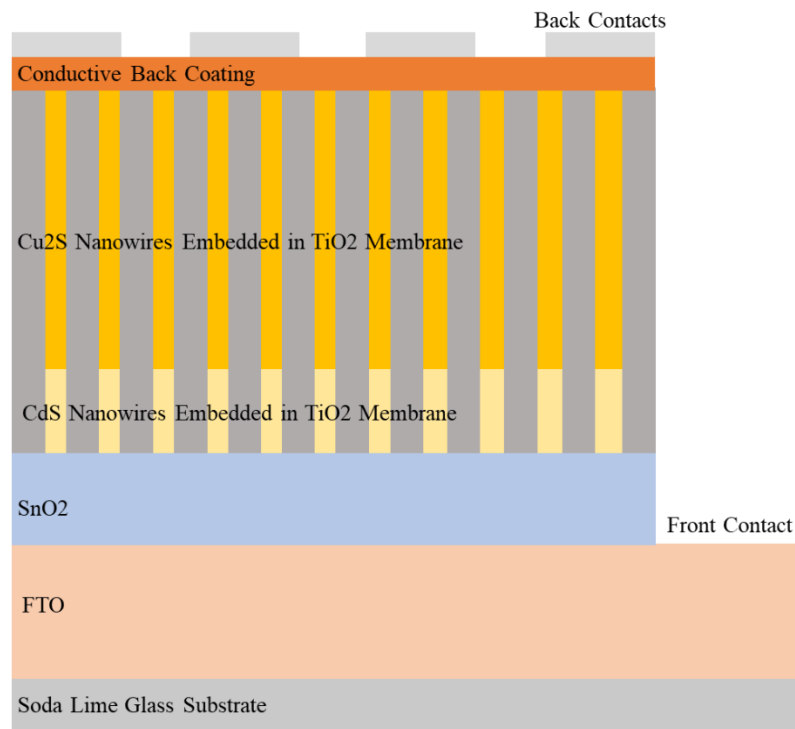


Figure 3.2: NW CdS/NW Cu₂S

3.2 Cleaning of Substrate

Soda lime glass coated with fluorine doped tin oxide (FTO) is ordered from MSE Supplies to act as the substrate. These samples must be thoroughly cleaned before any deposition to ensure that a uniform film with good adhesion can be deposited. The sample are first marked on the non-conductive side with a diamond tipped glass etching tool to ensure that the correct side is used during subsequent depositions. The sample are then suspended in a bath of acetone and sonicated for 30 minutes. This is followed by a sonication for 30 minutes suspended in a bath of isopropyl alcohol. Sample are then thoroughly rinses in deionized (DI) water and dried in a nitrogen flow.

3.3 Microwave Induced Plasma Etch

The now cleaned sample are placed in a vacuum chamber and are etched with an oxygen plasma for 3 minutes using the microwave induced plasma etching system in the Center for Nanoscale Science and Engineer (CENSE) at the University of Kentucky. This is done to remove any lingering contaminates. Once cooled, the samples are removed and a portion of the FTO is masked with foil so that it can be later used as a front contact.

3.4 RF Sputtering of SnO₂

100nm of intrinsic SnO₂ is deposited via RF sputtering using the AJA Phase II Sputtering system in the Center for Advanced Materials (CAM) at the University of Kentucky. This was done under based pressure of 7e-8 Torr and deposition pressure of 3e-3 Torr at a constant rate of 1.58 nm per minute. This layer is deposited due to its observed effects in CdS/CdTe solar cells as a buffer layer. In CdS/CdTe devices, the high resistivity of this film prevents diffusion of CdTe through a thin CdS layer. This leads to increased V_{oc} and FF [39]. It is assumed that this layer will have a similar effect in CdS/Cu₂S devices.

3.5 Deposition of Titanium Film

Due to the two thickness of porous TiO₂ templates required, two different methods of Ti deposition were used.

3.5.1 Nanowire CdS/Planar Cu₂S Device

150nm of Ti are sputtered onto the sample using the same system as the SnO₂ was deposited with. The same base and deposition pressures were also used. The rate was a constant 4.2 nm per minute. The foil masking is removed after deposition.

3.5.2 Nanowire CdS/Nanowire Cu₂S Device

Samples are shipped to LGA Thin Films to deposit 4μm of Ti via DC sputtering. The pressure and deposition rate were not recorded by the LGA Thin Films. The foil masking is removed after deposition.

3.6 Formation of Titania Nanotubes

Both Ti films are anodized in an electrolyte solution with the same recipe of .3 mL NH₄F (40% by volume, aqueous) and 97mL ethylene glycol. A PTFE beaker must be used for this process due to the precedence of fluorine which will attack a glass beaker. This beaker is thoroughly rinsed with isopropyl alcohol (IPA) followed by DI water and then dried in a nitrogen flow. A ½ inch magnetic stirrer is also rinsed in IPA followed by DI water and dried in a nitrogen flow. The clean stirrer is then placed in the bottom of the clean beaker. 97mL of ethylene glycol is then measured using a graduated cylinder and slowly added to the beaker. The beaker must then be slowly rotated at an angle to capture any droplets of ethylene glycol that have attached to the side of the beaker. The beaker is now placed on a stirring plate and the stirring speed is set to 500 rpm. .3mL NH₄F is then measured with a pipette and placed in the beaker. The solution is left to mix for 30 minutes before anodization occurs.

A 1in x 1in platinum plate is used as the counter electrode for anodization. This is stored in a .1M solution of hydrochloric acid (HCl) to prevent contamination. The Pt electrode is thoroughly rinsed with DI water and dried in a nitrogen flow prior to use. The Ti sample and Pt electrode are attached to copper clips separate by 1in and adjusted so that they are parallel. This ensures a uniform potential across the sample during anodization. Stirring speed is reduced to 200rpm and the electrodes are immersed in the solution to a depth such that a small portion of Ti on the sample is still above the solution. The positive lead of a power supply is connected to the sample and the negative lead to the Pt electrode. The power supply is then set to a constant supply of 50V and turned on.

The current over time is tracked using LabView and is used to know when the anodization is complete. Anodization is stopped when the current is observed to drop to near zero amperes. A typical current versus time curve can be seen below in figure 3.3.

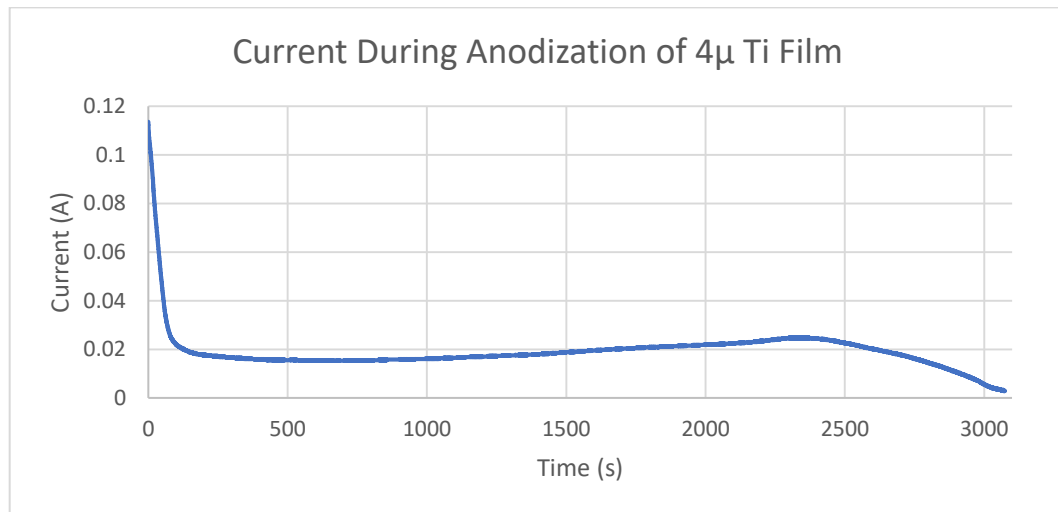


Figure 3.3: Current During Anodization

A SEM image of an anodized 150nm and 4 μ m sample can be seen in figures 3.4 and 3.5 respectively.

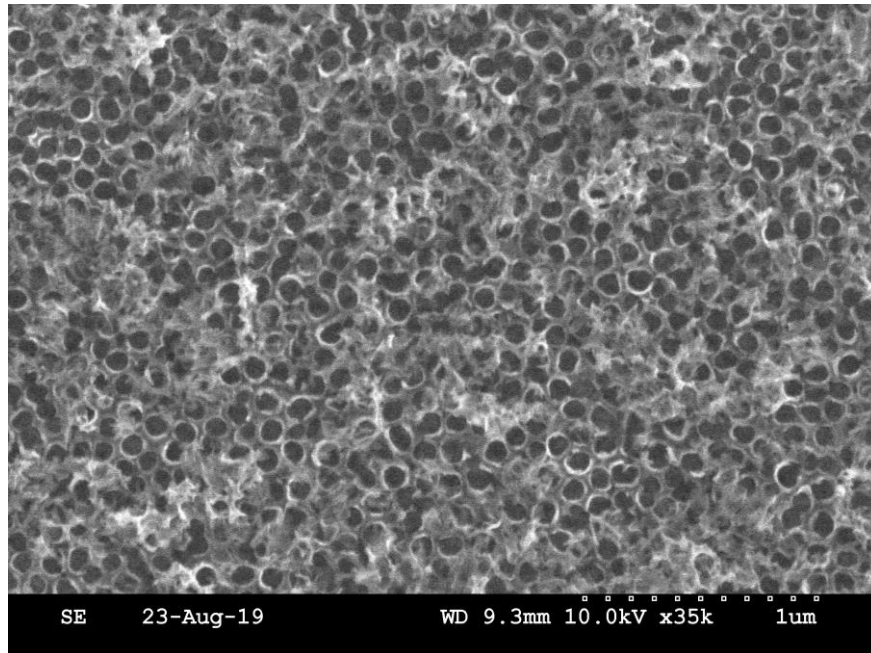


Figure 3.4: SEM Image of 150nm Anodized Ti Sample

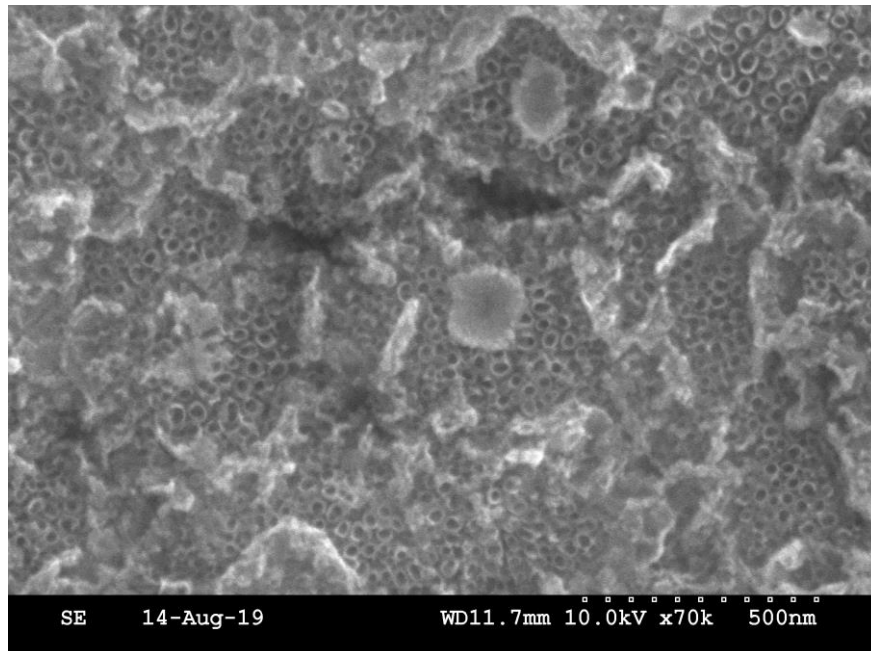


Figure 3.5: SEM Image of 4 μ m Anodized Ti Sample

The roughness present in the 4 μ m sample is likely due to the roughness of the film received from LGA Thin Films. This is thought to be due to a difference in substrate temperature during deposition compared to the 150nm Ti sample. A SEM image of the Ti before anodization can be seen in figure 3.6.

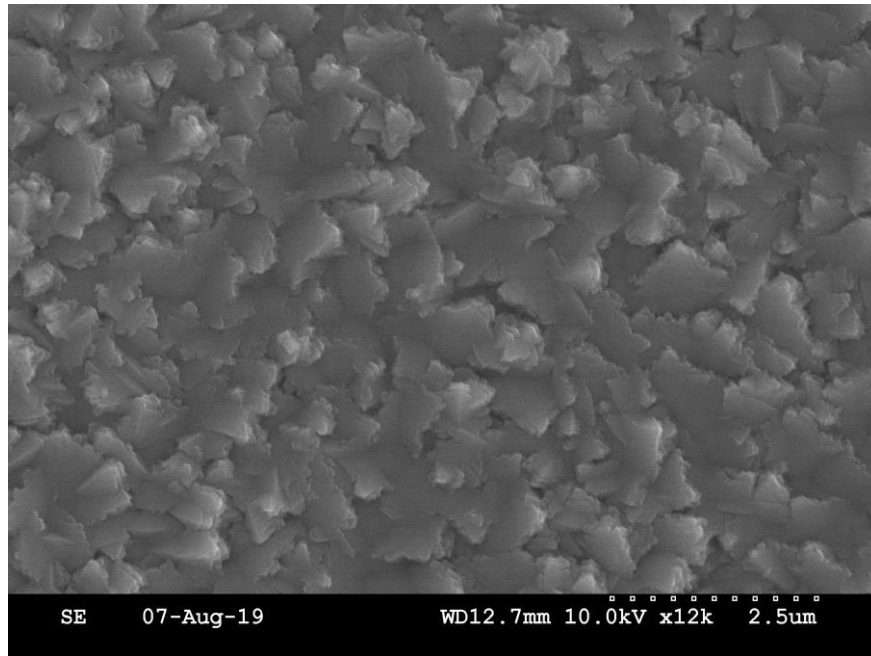


Figure 3.6: 4 μ m Ti Sample Before Anodization

3.7 Annealing of Ti Nanotubes

It is necessary to anneal the TiO₂ nanotubes in order to shift it from an amorphous crystal structure to anatase form. This is done by annealing the sample for two hours in an oxygen environment at 400°C. Converting to anatase phase significantly increases the conductivity of the TiO₂ [15]. This leads to lower series resistance in the final device.

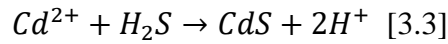
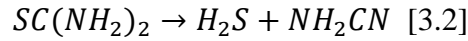
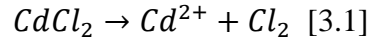
3.8 Electrodeposition of CdS

CdS is electrodeposited using a two electrode set up adapted from the Dharmadasa group's methods [16-18]. A glass beaker is rinsed with IPA followed by DI water and is dried in a nitrogen flow. A ½ in magnetic stirrer is cleaned in the same manner and is placed in the beaker. 50mL of DI water is measured and placed into the beaker. The beaker is then set on a hot plate with stirring speed set to 500 rpm and temperature to 80°C. Temperature is monitored with an IR thermometer. 1.1418g of thiourea ($\text{SC}(\text{NH}_2)_2$) is then added to the DI water followed by 2.0133g cadmium chloride hydrate ($\text{CdCl}_2 \times \text{H}_2\text{O}$). The pH of the solution is then adjusted with dilute hydrochloric acid (HCl) and ammonium hydroxide (NH_4OH) to $2.7 \pm .1$. This solution is then allowed to mix for at least 30 minutes and up to an hour before electrodeposition.

The same Pt plate that was used to anodize Ti is used as the counter electrode for electrodepositing CdS. This electrode is thoroughly rinsed in DI water and dried in a nitrogen flow. The sample and Pt electrode are attached to copper clips separated by 1in and adjusted so that they are parallel. The stirring speed is lowered to 100 rpm and the electrodes are placed into solution. The sample must sit in solution for at least 1 minutes to allow for the nanotubes to fill with the solution. The positive clip of a power supply is attached to the Pt and the negative clip attached to the sample. The power supply is set to a constant voltage of .82V and turned on. The electrodeposition is allowed to go for 5 hours to deposit sufficient CdS. The sample is removed from solution after the required amount of time and gently rinsed with DI water as well as being dried in nitrogen stream.

The reaction by which CdS is electrodeposited is as follows. The CdCl_2 breaks down to Cd^{2+} ions in the acidic solution, the thiourea breaks down to form H_2S , and

lastly the Cd^{2+} combines with the H_2S to form CdS and two spare H^+ ions [16]. There are other reactions that occur in the solution, but these are not of interest as they do not directly affect CdS formation. These reactions are summarized in the following set of equations:

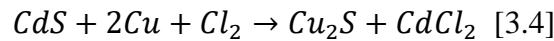


3.9 Annealing of CdS Nanowires

The CdS nanowires are now annealed to reduce mechanical stress and improve quality of the CdS itself [16,17]. The sample is annealed in open air at a temperature of 450°C for 15 minutes to accomplish this.

3.10 Formation of Cu_2S

Cu_2S is formed by the “Clevite Wet Process” in which the CdS is dipped into a hot saturated solution of copper ions with ammonium chloride and a reducing agent [19-22]. The copper ions diffuse into the CdS where they replace the Cd in the following reaction:



A solution is prepared with copper (1) chloride (CuCl), ammonium chloride (NH_4Cl), and oxalic acid ($\text{C}_2\text{H}_2\text{O}_4$). Due to its oxidation when left in open air, CuCl must be bleached before it is used. This is done by placing CuCl in a filter and pouring .1M

molar HCl over it until it regains its pure white color. It is then rinsed with acetone to help it dry out.

A glass beaker and ½ inch magnetic stirrer are cleaned with the same process as the anodization and electrodeposition. A solution is then prepared in DI water by adding .05M oxalic acid as the reducing agent. This remove free oxygen from the solution, which must be done to prevent the re-oxidation of CuCl when it is added to the solution. An older technique used to remove oxygen is bubbling an inert gas through the DI water [19]. Then .1M ammonium chloride is added followed by .06M of bleached CuCl. The pH is then adjusted to $1.5 \pm .1$ with HCl and NH₄OH. Stirring speed is set to 500 rpm and temperature to 100°C during this process. Before the CdS is dipped, it is etch for 10s in .5M HCl to produce a surface roughness that aids in conversion [20,23]. The CdS is then dipped into the Cu ion solution for 30s. After this, the sample is gently rinse in DI water to remove the CdCl₂ that forms during the reaction.

3.11 Annealing of Cu₂S

The sample is then place in a vacuum oven where it is placed under a vacuum of 30 inHg. The sample is then annealed at 200°C for 20 minutes. This process serves the dual purpose of improving the junction by driving the copper deeper into the device and relieving any mechanical stress that has built up during previous depositions.

3.12 Formation of Back Contacts

Contact are formed by using RF sputtering to deposit a thin layer of Cu over the entirety of the Cu₂S. This will form the electrical connection between the Cu₂S nanowire

that are separated by the titania template. Additionally a grid of chromium contacts are be thermally evaporated on the Cu layer to form good ohmic contact. These contact also serve the purpose of reflecting back most of the light that is not absorbed on the first pass.

CHAPTER 4: SIMULATION

Simulations of both device structures has been carried out under numerous different conditions in order to find the highest efficiency possible for both NW CdS/planar Cu₂S and NW CdS/NW Cu₂S solar cells. All simulation work was done using SCAPS-1D (solar capacitance simulator in 1 Dimension) [24]. SCAPS is a solar simulation program that was originally developed at the University of Gent for CdTe and CuInSe₂ families of solar cells. The program has seen many modification and additions that now allow it to be widely used throughout the solar research community for various type of solar cells, including: silicon (amorphous and crystalline), perovskite [25], CIGS [26], GaAs [27], and CuSbS₂ [28]. It has been determined that due to Cu₂S's structural similarities to the aforementioned materials, especially CuSbS₂, SCAPS can provide an accurate simulation of a Cu₂S absorber solar cell.

SCAPS allows for simulations of structures with up to 7 different semiconductor layers stacked on each other with control of a number of the material parameters. This includes: E_g , χ , ϵ , N_C , N_V , v_{thn} , v_{thp} , μ_n , μ_p , N_A , N_D , all traps (defects) N_t . All of these can be either held constant or graded throughout the layer. Several distinct types of recombination are also taken into account, such as: direct band-to-band, auger, and Shockley-Read-Hall recombination. Additionally, defect levels can be manually added for various charge types, distributions, and energy levels. SCAPS also can take into account the effect of intraband tunneling and tunneling in/from interface states. Optical filters, such as an anti-reflective coating, can be added in the contact layers.

SCAPS allows for various spectra of illumination to be used, including AM0, AM1.5D, AM1.5G, AM1.5 Gediton2, monochromatic, and white. For the purposes of this paper, only AM1.5G is used as this is the global average solar spectrum for flat plate solar panel modules. AM0 is the spectrum in outer space and AM1.5D is used for solar concentrators. The difference in spectra can be seen in figure 4.1.

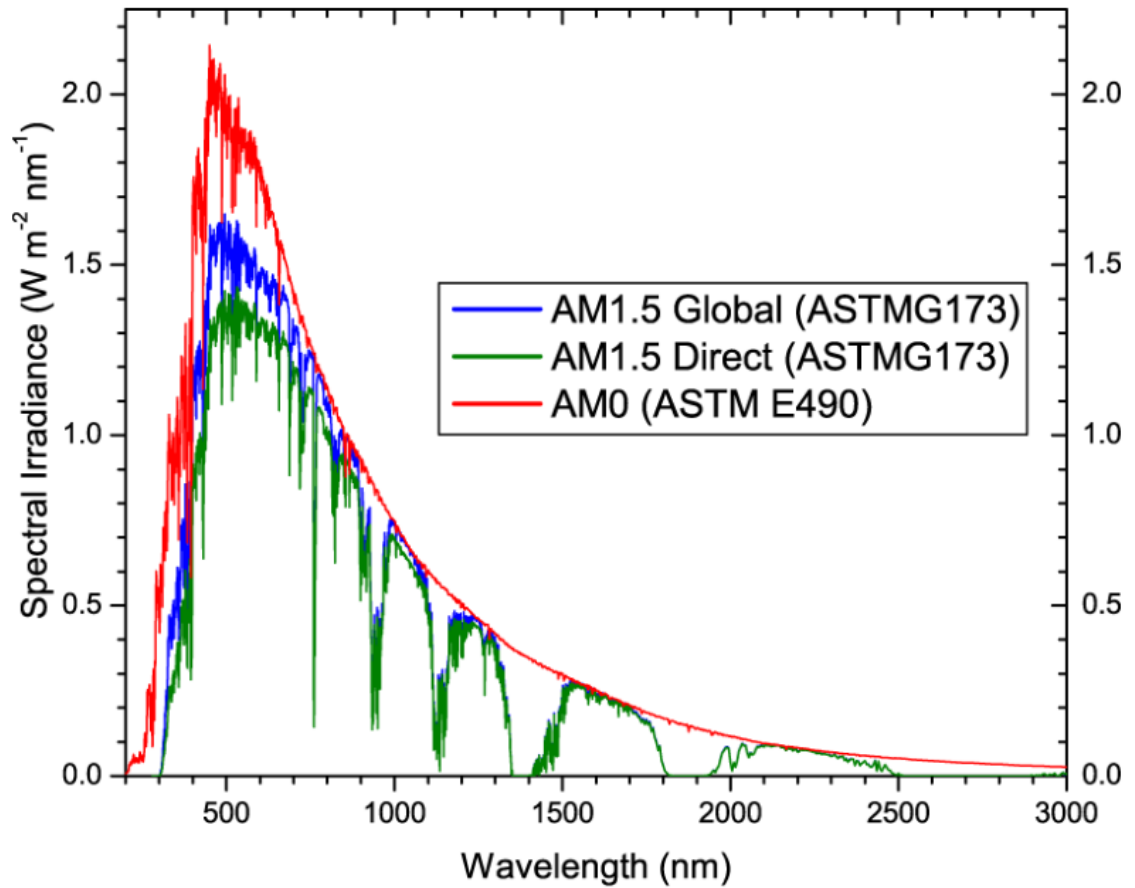


Figure 4.1: Difference in Solar Spectra [29]

SCAPS takes in all of this information and calculates: energy bands, carrier concentrations and currents at a given working point (voltage, frequency, and temperature), J - V characteristics, AC characteristics (C and G as function of V and/or f), spectral response (also with bias light or voltage) [24].

This is accomplished by solving the Poisson (eq. 5.1) and continuity equations (eq. 5.2 and 5.3) using a numerical approach across a predefined mesh of points.

$$\frac{\partial}{\partial x} \left(\epsilon \frac{\partial \Psi}{\partial x} \right) = \frac{-q}{\epsilon_0} \left(-n + p - N_A + N_D + \frac{1}{q} \rho_{defect}(n, p) \right) \quad [5.1]$$

$$-\frac{\partial j_n}{\partial x} + G - U_n(n, p) = \frac{\partial n}{\partial t} \quad [5.2]$$

$$-\frac{\partial j_p}{\partial x} + G - U_p(n, p) = \frac{\partial p}{\partial t} \quad [5.3]$$

Poisson's equation describes the electric field that arises from different concentrations of holes, p and N_A , and electrons, n and N_D , in the device. The continuity equations show that the current density must be equal to the amount of generated carriers, G , minus the total amount of carriers lost to recombination, U . A Gummel iteration is used with Newton-Raphson sub steps to solve these equations numerically. This method works very well in most cases as long as the initial iteration is not extremely far off. Unfortunately, it can also result in convergence failures if the initial iteration is off or if the mesh of points that the equations are solved over has any discontinuities.

Recombination at the interface states is modeled using the Pauwels-Vanhoutte theory, which is an extension of Shockley-Read-Hall theory [30]. This theory takes into account not just direct recombination, but also cross recombination. Four different recombination paths exist at the interface under this theory: 1) The electrons in the conduction band of the window layer can recombine with the holes in the valence band of the window layer, 2) The electrons in the conduction band of the window layer can recombine with the holes in the valence band of the absorber layer, 3) The electrons in

the conduction band of the absorber can recombine with the holes in the valence band of the absorber layer, and 4) The electrons in the conduction band of the absorber can recombine with the holes in the valence band of the window layer [31]. That is to say, electrons can cross over into the other layer to recombine as opposed to just being able to recombine in the layer they start in. An example of recombination types 3 (left) and 2 (right) can be seen in figure 4.2

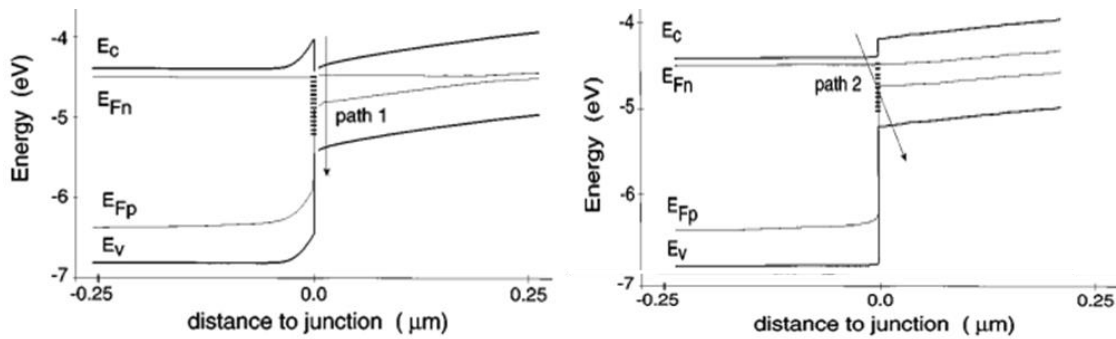


Figure 4.2: Example of Two Paths of Recombination at the Interface [31]

4.1 Simulating With SCAPS-1D

SCAPS has several different menus to control the simulations. This section will explain the basic functionality of each one used for the simulations done for this paper.

Figure 4.3 shows the basic structure of a solar cell in SCAPS.

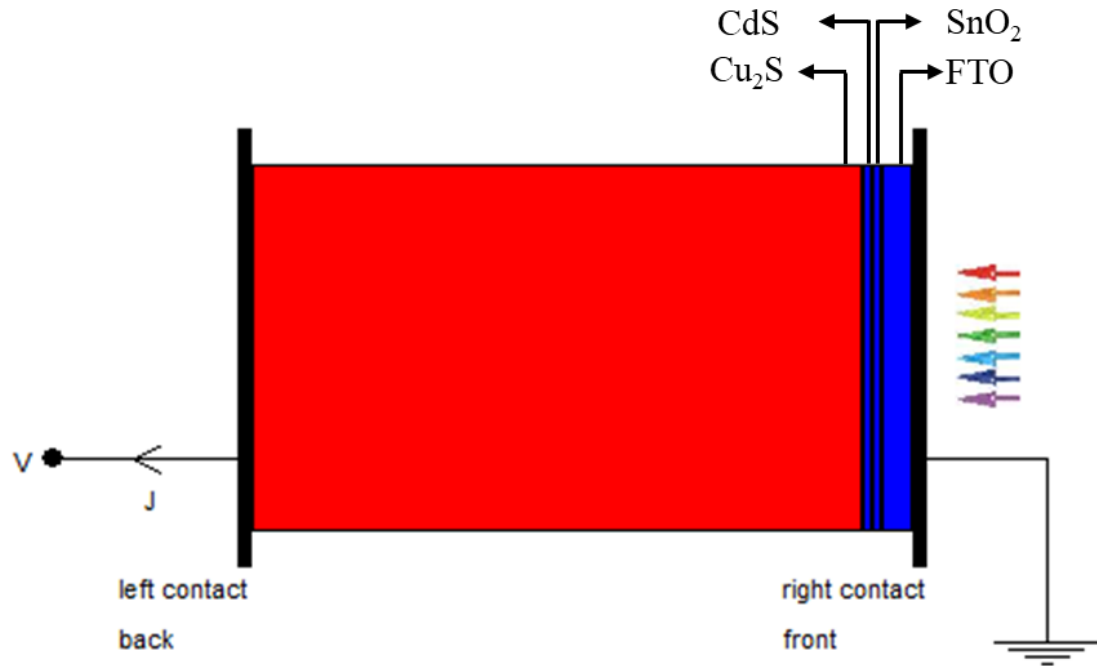


Figure 4.3: Basic Solar Cell Structure in SCAPS

Due to how SCAPS was programmed, the p-type absorber region must be connected to the left contact in order to form a p-n junction as opposed to a n-p junction. An n-p junction results in non-uniform current and stability issues. The materials chosen for the two device designs can be seen in figure 4.3, but the nanostructures cannot. SCAPS was not designed to directly handle nanostructured solar cells but by inputting adjusted parameters based on how expect to nanostructures behave, it is possible to use SCAPS to simulate them. These will be explained in section 4.2.

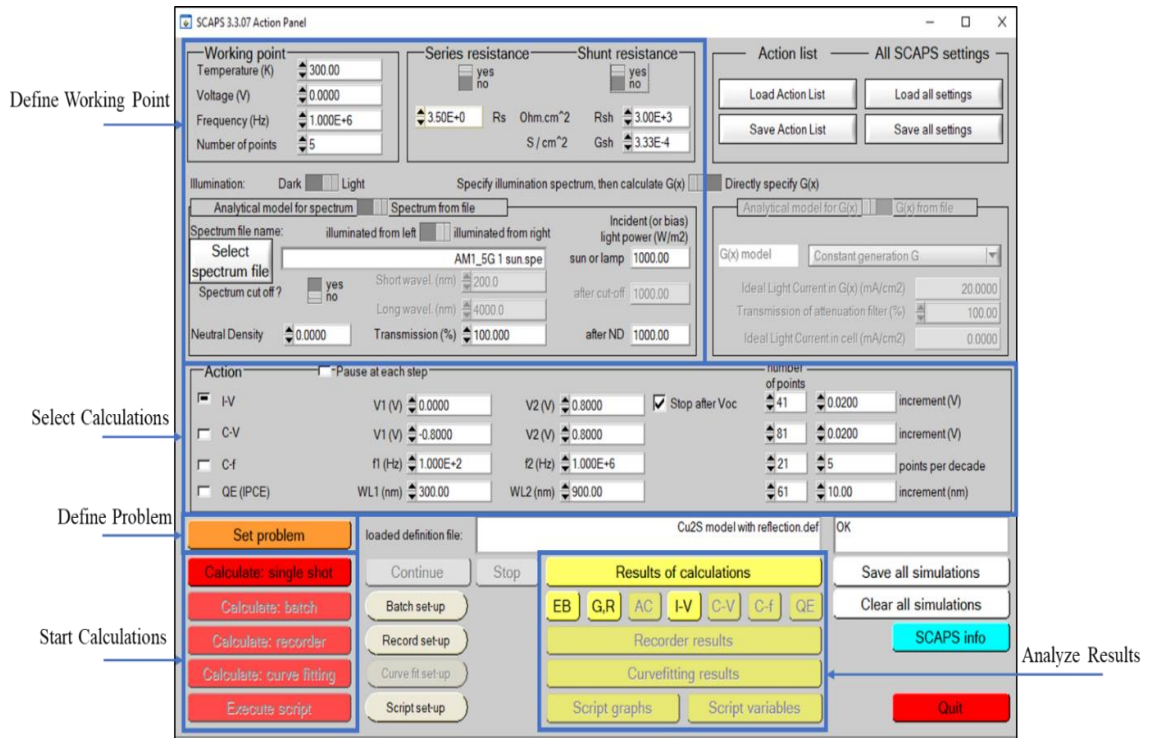


Figure 4.4: SCAPS Action Panel

Figure 4.4 shows the SCAPS action panel. This is where all general setup for the simulation is done. You must first define your working point. The temperature working point affects every type of simulation as it affects the density of state in the valence and conduction bands (N_v and N_c), the hole and electron thermal velocities ($v_{th,n}$ and $v_{th,p}$), and the thermal voltage (kT). The voltage working point is disregarded in I-V and C-V simulations but is used as the DC bias in C-f and quantum efficiency ($QE(\lambda)$) simulations. The frequency working point is disregarded in I-V, C-f, and $QE(\lambda)$ simulations but is used as the frequency in C-V simulations. Series and shunt resistance are used in all simulations. The illumination working point is used for all simulations. It can be set to a multitude of different spectra or even to dark. For this paper, the only

working point of interest are the temperature and illumination. In all simulations, temperature was set to the standard room temperature of 300K and the illumination set to the standard AM1.5 spectrum.

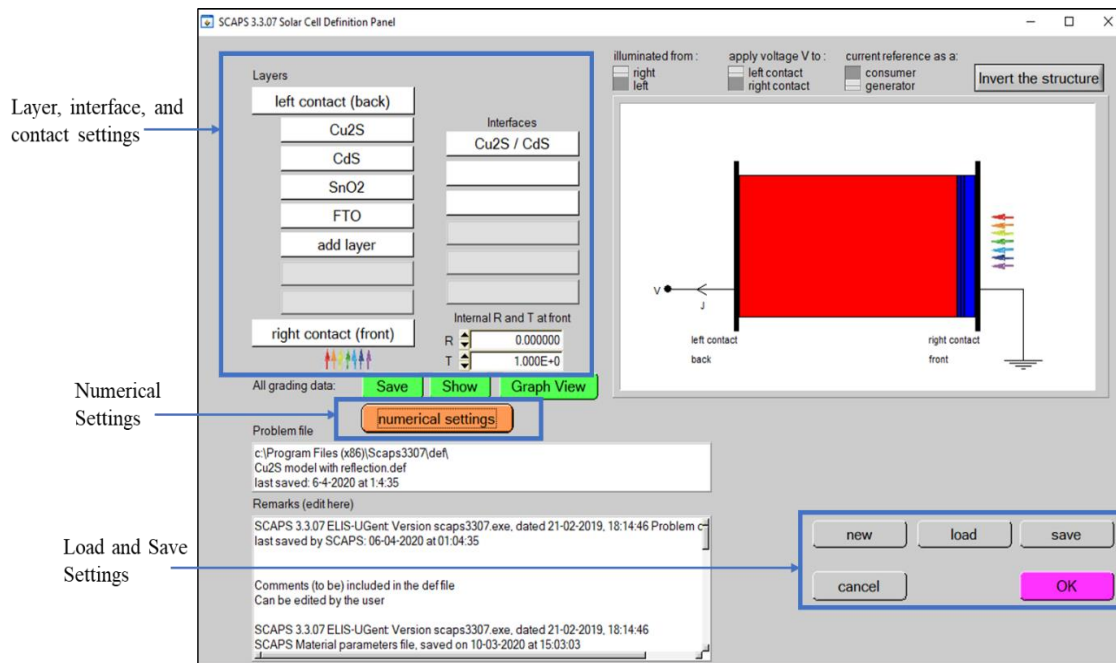


Figure 4.5: SCAPS Solar Cell Definition Panel

Figure 4.5 shows the SCAPS solar cell definition panel. Here, the user can define up to 7 semiconductor layers and the interfaces between them. The definitions of the contact can also be adjusted here. Additionally, the numerical setting for the simulations themselves can be adjusted here to the user's preference. Models of all these setting can be saved and loaded through this panel as well.

The top right of this panel show the solar cell as it is currently defined. Red regions are p-type semiconductors and blue regions are n-type semiconductors. The direction of illumination can be controlled as well as where to apply voltage to and

whether the current should be referenced as a generator or consumer. Changing these parameters will affect how the I-V curve will appear after the simulation.

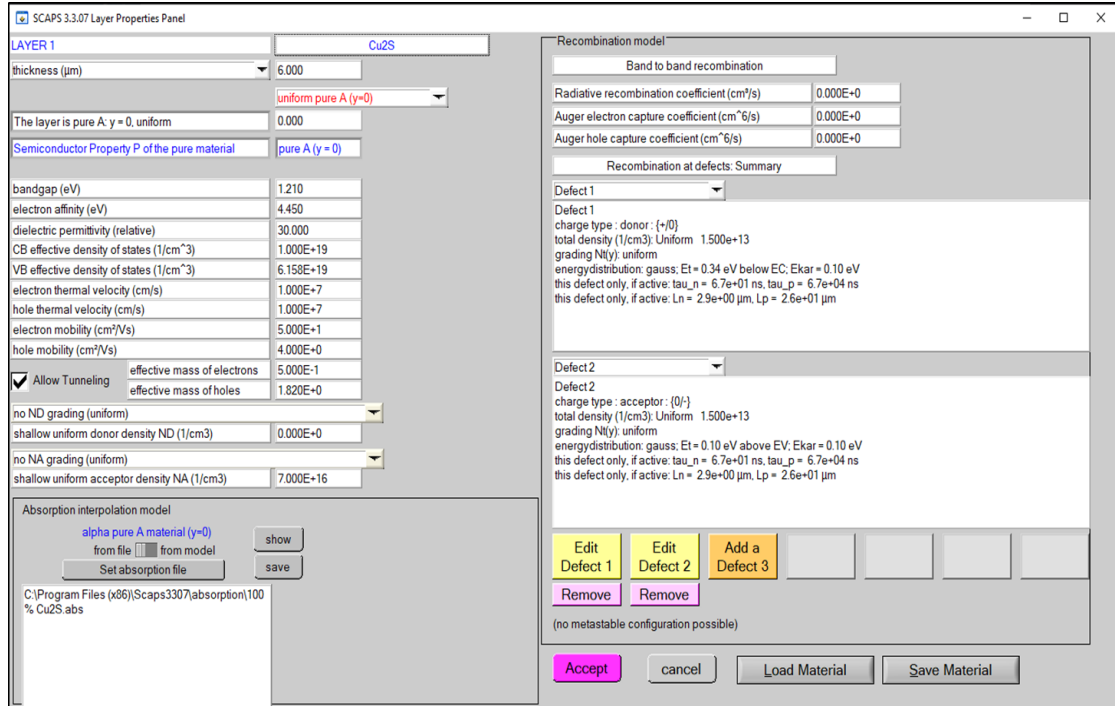


Figure 4.6: SCAPS Layer Properties Panel

Figure 4.6 shows the SCAPS layer properties panel. Here, the user defines the properties for each semiconductor layer. This includes: thickness, any grading desired, bandgap (E_g), electron affinity (χ), relative dielectric permittivity (ϵ), conduction band effective density of states (N_c), valence band effective density of states (N_v), electron thermal velocity ($v_{th\ n}$), hole thermal velocity ($v_{th\ p}$), electron mobility (μ_n), hole mobility (μ_p), effective mass of electrons (m_e), effective mass of holes (m_p), donor density (N_D), and acceptor density (N_A). Lastly the absorption profile for the material show the absorption coefficient of the material versus wavelength. Band to band recombination can also be defined here through the radiative recombination coefficient, auger electron

capture coefficient, and auger hole capture coefficient. Additionally, defects can be added to the material. This is shown in figure 4.7.

The image shows the 'SCAPS 3.3.07 Defect Properties Panel' window. The title bar indicates the material is 'Cu2S' and the defect is 'Defect 1 of Cu2S'. The panel is divided into several sections for defining defect properties.

Property	Value
defect type	Single Donor (0/+)
capture cross section electrons (cm ²)	1.000E-13
capture cross section holes (cm ²)	1.000E-16
energetic distribution	Gauß
reference for defect energy level Et	Below EC
energy level with respect to Reference (eV)	0.340
characteristic energy (eV)	0.100

Below these fields, there are options for 'no Nt grading (uniform)' and 'Nt total (1/cm3)' (1.500E+13) and 'Nt peak (1/eV/cm3)' (8.463E+13). The 'Optical capture of electrons' section includes a checkbox for 'From model' (checked) and 'From file', and a table of optical properties:

Property	Value
refractive index (n)	3.000
effective mass of electrons (rel.)	1.000E+0
effective field ratio	1.00E+0
cut off energy (eV)	10.00

The 'Optical capture of holes' section is identical, also with 'From model' checked. At the bottom, there are 'accept' and 'cancel' buttons.

Figure 4.7: SCAPS Defect Properties Panel

Figure 4.7 shows the SCAPS defect properties panel. Here, the user can define the defect type, capture cross section for both electrons and holes, the energy level of traps, and the energy distribution of traps. The trap distribution can be defined as being single, uniform, gaussian, or CB tail. These distributions are modeled by the following equations in figure 4.8. Additionally, the optical capture of electrons and holes can be simulated.

	Range	$N_t(E) = \dots$	$N_{\text{tot}}(N_{\text{peak}})$
Single	$[E_t; E_t]$	$N_{\text{tot}} \times \delta_{E_t}$	
Uniform	$\left[E_t - \frac{E_c}{2}; E_t + \frac{E_c}{2}\right]$	N_{peak}	$N_{\text{tot}} = E_c N_{\text{peak}}$
Gauss	$\left[E_t - \frac{w_G}{2} E_c; E_t + \frac{w_G}{2} E_c\right]$	$N_{\text{peak}} \times \exp\left[-\left(\frac{E - E_t}{E_c}\right)^2\right]$	$N_{\text{tot}} = E_c N_{\text{peak}}$
CB tail	$[E_t - w_t E_c; E_t]$	$N_{\text{peak}} \times \exp\left(\frac{E - E_t}{E_c}\right)$	$N_{\text{tot}} = E_c N_{\text{peak}}$

Figure 4.8: Energy Distribution Options for Traps [24]

SCAPS 3.3.07 Interface Defect Properties Panel

Defect 1 of Cu2S / CdS interface

defect type	acceptor
capture cross section electrons (cm ²)	1.00E-13
capture cross section holes (cm ²)	1.00E-16
energetic distribution	gauss
reference for defect energy level Et	above the highest EV
energy with respect to Reference (eV)	0.810
characteristic energy (eV)	0.100
total density (integrated over all energies) (1/cm ²)	1.00E+12
density at peak energy (1/cm ² .eV)	5.64E+12

☒ Allow tunneling to interface traps

Relative mass of electrons	5.000E-1
Relative mass of holes	1.820E+0

accept cancel

Figure 4.9: SCAPS Interface Defect Properties Panel

The user is also able to define defect states at the interface between any two semiconductor layers. This can be seen in figure 4.9. The defect type can be specified as

well as the capture cross section for electrons and holes, the energy level of traps, and the energy distribution of traps. The energy distributions available for simulation are the same as those available for defects in a material as shown in figure 4.8. Additionally, tunneling to interface traps can be simulated by inputting the relative mass of electrons and holes. Interface recombination is based on Pauwels-Vanhoutte theory [30].

Left Contact (Back)

Electrical properties

Thermionic emission / surface recombination velocity (cm/s) :

electrons $1.00E+5$

holes $1.00E+7$

Metal work function (eV) 5.4844 or ☐ flat bands

Majority carrier barrier height (eV) :

relative to EF 0.1756

relative to EV or EC 0.0000

☐ Allow contact tunneling

Effective mass of electrons $1.00E+0$

Effective mass of holes $1.00E+0$

Optical properties

optical filter ☒

Filter Mode ☒ transmission ☐ reflection

Filter Value 0.900000

Complement of Filter Value $1.0000E-1$

From Value ☐

From File ☐

Select Filter File

OK cancel

Figure 4.10: SCAPS Contact Properties Panel

Figure 4.10 shows the SCAPS contact properties panel. Here, the user can define different properties for both the front contact and the back contact. The recombination velocity of electrons and holes can be set here as well as the metal work function. The use

can also choose to enable flat bands. With this setting, SCAPS the metal work function, Φ_m , at every temperature such that flat band conditions are dominant. SCAPS takes into account both shallow doping density as well as defects in the adjacent layers to determine this. Contact tunneling can also be allowed or not depending on user preference. Additionally, optical filters can be applied to both contacts. This can be a reflective or transmissive filter defined by a flat value or a file of specific values at each wavelength.

As previously mentioned, SCAPS has several different modes of simulation. This paper only makes use of I-V simulations as that is the simulation that reports V_{oc} , J_{sc} , FF, and eta which are the primary values of interest when determining the performance of a solar cell. A sample output of an I-V simulation can be seen in figure 4.11.

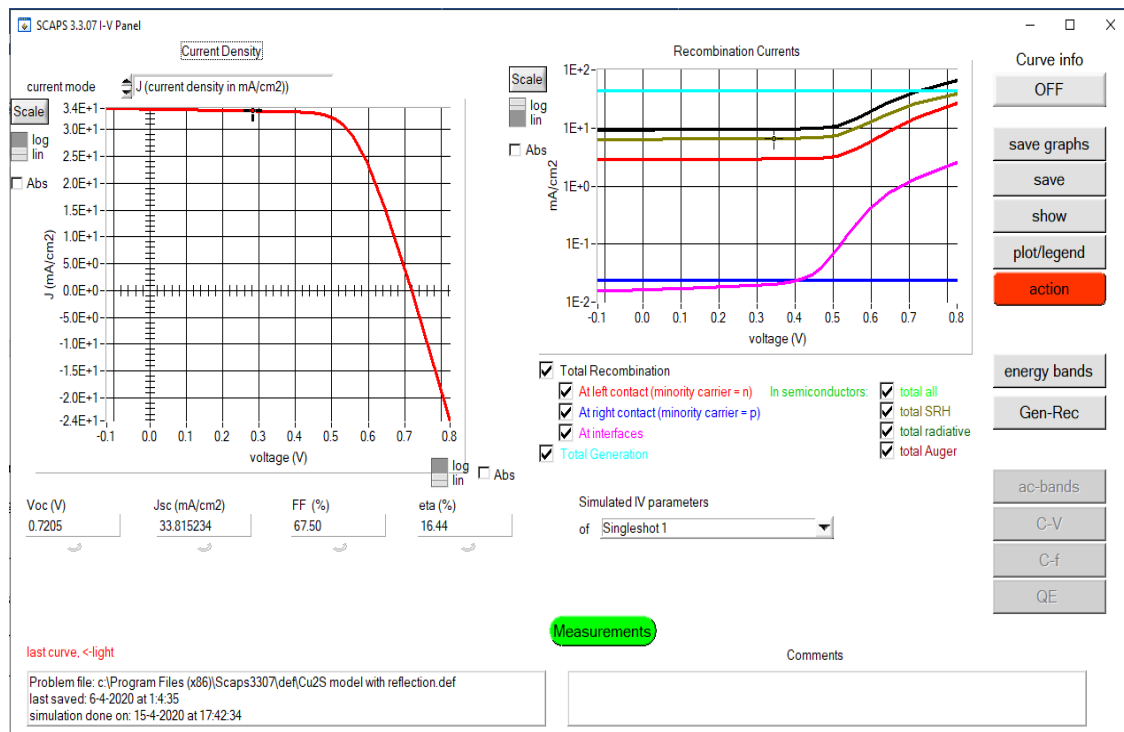


Figure 4.11: SCAPS I-V Simulation Output

4.2 Theoretical Models

The theoretical models and parameters used to define each model in SCAPS are described in the following sections.

4.2.1 Nanowire CdS/Planar Cu₂S Model

The nanowire CdS/planar Cu₂S device is modeled by adjusting the bandgap and absorption profile of the CdS layer. Previous work by the group has demonstrated that placing CdS into nanotubes shifts its bandgap from 2.4 eV to approximately 3.5 eV [32-34]. These nanowires were fabricated with a diameter of approximately 50 nm, which is greater than the Bohr Radius of CdS. The shift in bandgap is attributed to stacked nanodisks of thickness lower than the Bohr Radius forming nanowires. CdS is modeled as having a bandgap 3.5 eV for nanowires of any width.

The absorption profile of nanowire CdS in a TiO₂ template is modeled by interpolating the absorption spectrum of a planar CdS sample with the absorption spectrum of TiO₂. By defining CdS coverage as a percentage of the total surface covered by CdS nanowire, the following equation can be used to find the absorption spectrum of any percent coverage of CdS. X represents the percentage of the surface covered with CdS nanowires and A is the absorption spectrum for a material.

$$X * A_{Planar\ CdS} + (100\% - X) * A_{TiO_2} = A_{X\ Coverage\ CdS\ Nanowires} \quad [4.1]$$

This equation has been verified experimentally in previous work using UV-vis spectroscopy [14]. Figure 4.12 demonstrates that this equation is a good approximation of

the absorption spectrum of CdS nanowires with a coverage of 32%. Due to this, the equation has been used to model a much wider range of CdS coverages.

Absorption vs Wavelength for 32% CdS Coverage Experimental vs Theoretical

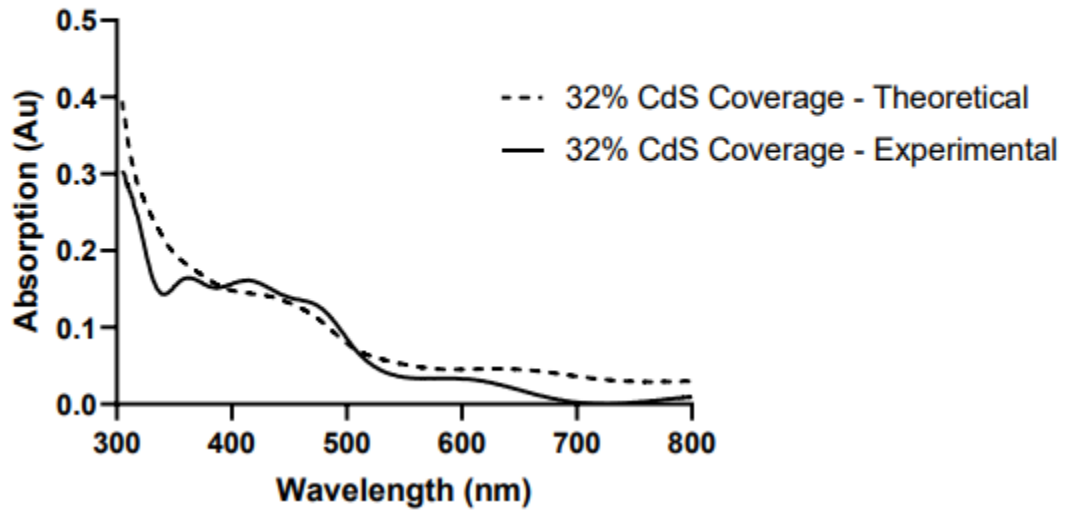


Figure 4.12: Experimental Verification of Nanowire CdS Absorption Spectrum [14]

The absorption spectrum is then converted to an absorption coefficient so that SCAPS can use it for modeling it. The following figures show the range of CdS coverages modeled and their associated absorption coefficients.

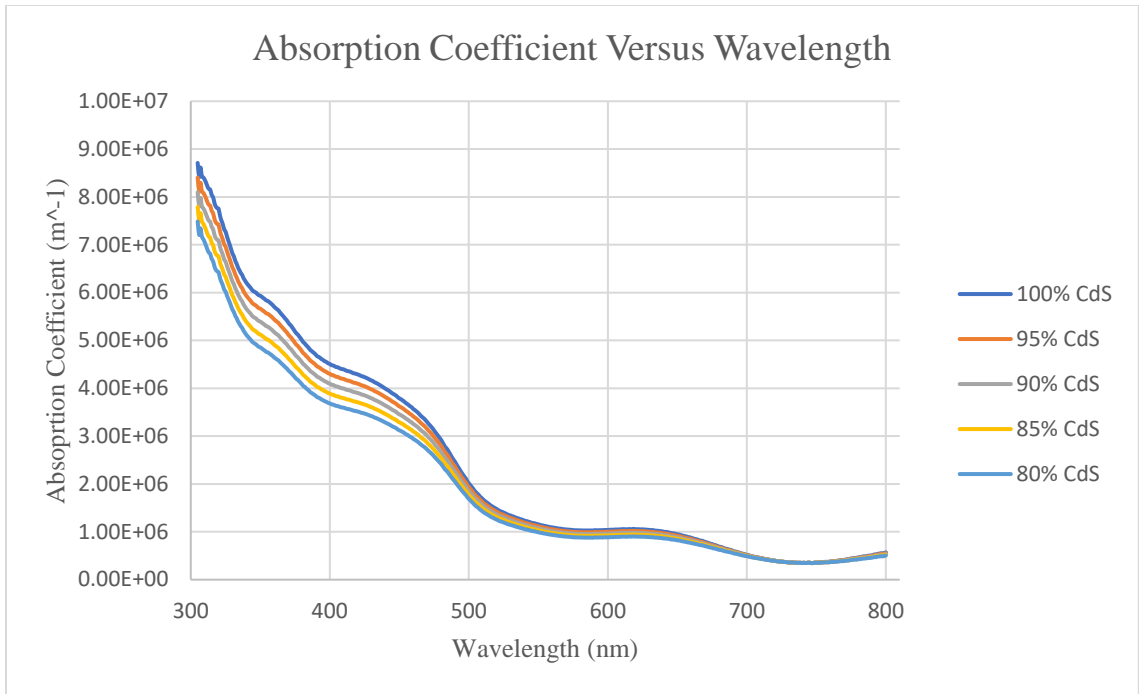


Figure 4.13: Model of Absorption Coefficient for CdS Nanowire Coverage 100%-80%

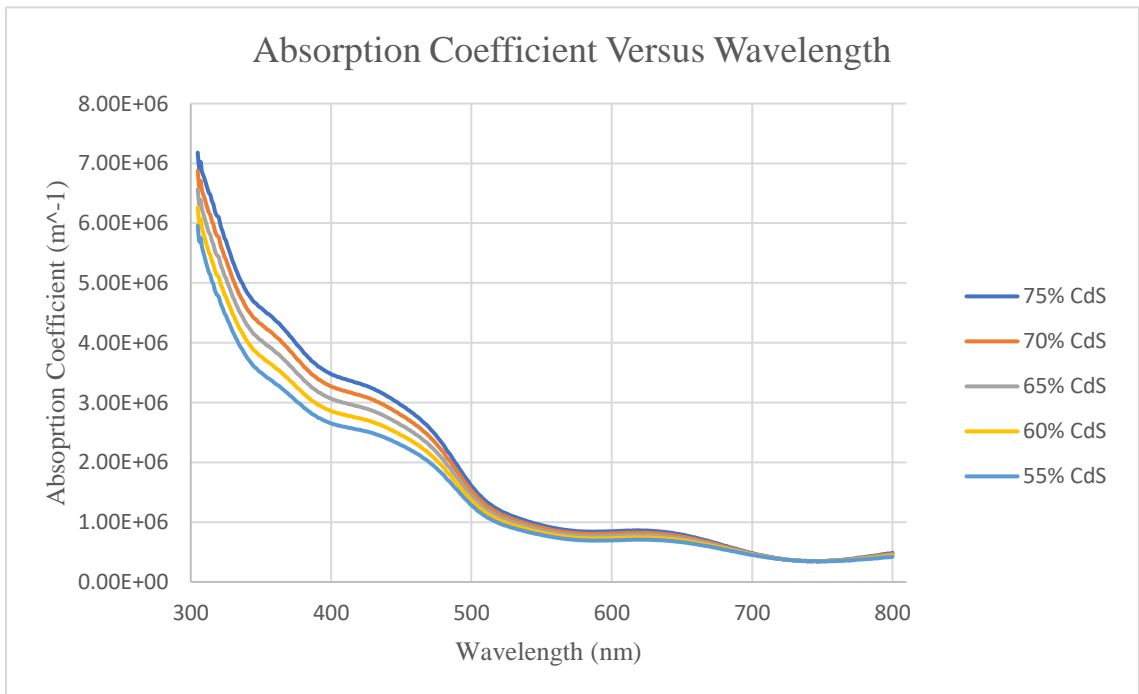


Figure 4.14: Model of Absorption Coefficient for CdS Nanowire Coverage 75%-55%

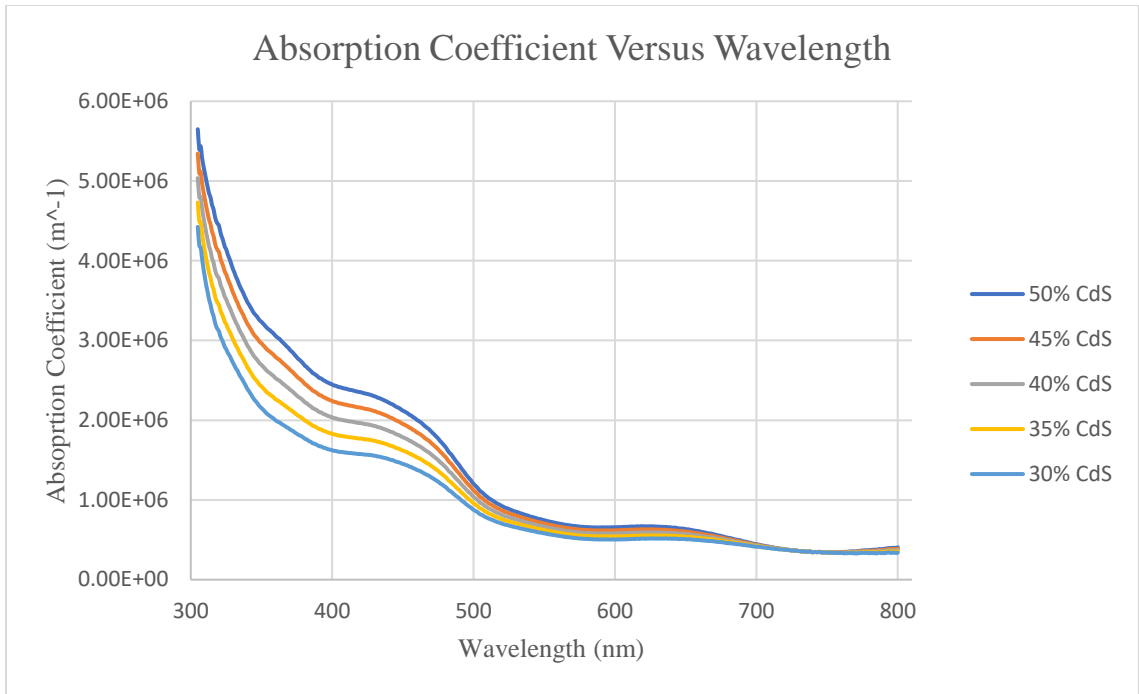


Figure 4.15: Model of Absorption Coefficient for CdS Nanowire Coverage 50%-30%

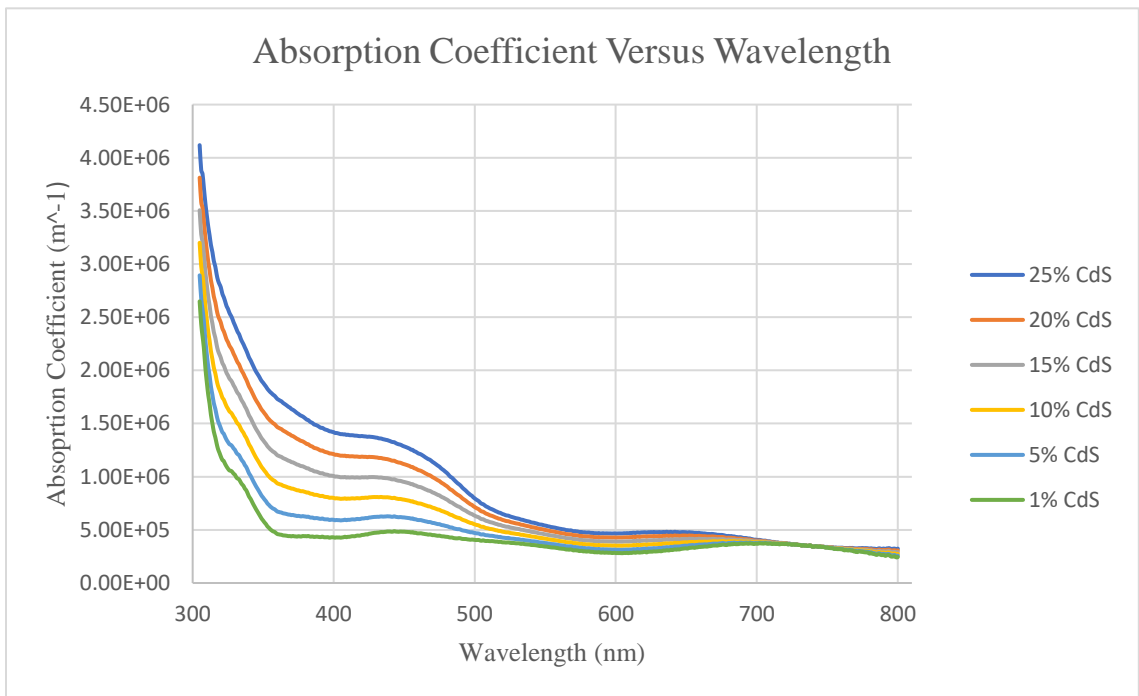


Figure 4.16: Model of Absorption Coefficient for CdS Nanowire Coverage 25%-1%

Additionally, the number interface states between the nanowire CdS layer and planar Cu₂S layer is assumed to decrease linearly with CdS coverage. That is, CdS coverage of 1% has 1% of the interface states found between planar (100%) CdS and Cu₂S.

The base parameters used for the nanowire CdS/planar Cu₂S device are as follows:

Table 4.1 Material Parameters of Left (Back) Contact

Back Contact	Parameter	Value
	Thermionic Emission/Surface Recombination Velocity of:	
	Electrons	1.00E+5 cm/s
	Holes	1.00E+7 cm/s
	Calculate Flat Band Conditions Instead of Providing Φ_m	
	Optical Properties	
	Filter Mode	Reflection
	Filter Value	.900
	Complement of Filter Value	.100

Table 4.2 Material Parameters of Cu₂S Layer

Cu ₂ S	Parameter	Value
	Thickness (μm)	6
	Bandgap (eV)	1.21
	Electron Affinity (eV)	4.45
	Dielectric Permittivity (relative)	30
	CB Effective Density of States (cm ⁻³)	1.00E+19
	VB Effective Density of States (cm ⁻³)	6.158E+19
	Electron Thermal Velocity (cm/s)	1.00E+7
	Hole Thermal Velocity (cm/s)	1.00E+7
	Electron Mobility (cm ² /Vs)	50.00E+1
	Hole Mobility (cm ² /Vs)	4.000E+0
	Effective Mass of Electrons	5.00E-1
	Effective Mass of Holes	1.82E-1
	Shallow Uniform Acceptor Density N _A (cm ³)	7.00E+16

Table 4.3 Parameters of Defect 1 of Cu₂S

Cu ₂ S Defect 1	Parameter	Value
	Defect Type	Single Donor
	Capture Cross Section Electrons (cm ²)	1.00E-13
	Capture Cross Section Holes (cm ²)	1.00E-16
	Energetic Distribution	Gauß
	Reference for Defect Energy Level E _t	Below E _c
	Energy Level with Respect to Reference (eV)	.340
	Characteristic Energy (eV)	.1
	N _t total (cm ⁻³)	1.5E+13
	N _t Peak (cm ⁻³ /eV)	8.463E+13

Table 4.4 Parameters of Defect 2 of Cu₂S

Cu ₂ S Defect 2	Parameter	Value
	Defect Type	Single Acceptor
	Capture Cross Section Electrons (cm ²)	1.00E-13
	Capture Cross Section Holes (cm ²)	1.00E-16
	Energetic Distribution	Gauß
	Reference for Defect Energy Level E _t	Below E _v
	Energy Level with Respect to Reference (eV)	.1
	Characteristic Energy (eV)	.1
	N _t total (cm ⁻³)	1.5E+13
	N _t Peak (cm ⁻³ /eV)	8.463E+13

Table 4.5 Parameters of Cu₂S/CdS Interface Defect

Cu ₂ S/CdS Interface	Parameter	Value
	Defect Type	Acceptor
	Capture Cross Section Electrons (cm ²)	1.00E-13
	Capture Cross Section Holes (cm ²)	1.00E-16
	Energetic Distribution	Gauß
	Reference for Defect Energy Level E _t	Above Highest E _v
	Energy Level with Respect to Reference (eV)	.81
	Characteristic Energy (eV)	.1
	Total Density [integrated over all energies] (cm ⁻²)	1.00E+12
	Density at Peak Energy (cm ⁻² /eV)	5.64E+12
	Relative Mass of Electrons	5.00E-1
	Relative Mass of Holes	1.82E+0

Table 4.6 Material Parameters for CdS Layer

CdS	Parameter	Value
	Thickness (μm)	.100
	Bandgap (eV)	3.2
	Electron Affinity (eV)	4.1
	Dielectric Permittivity (Relative)	9
	CB Effective Density of States (cm^{-3})	2.30E+18
	VB Effective Density of States (cm^{-3})	1.70E+19
	Electron Thermal Velocity (cm/s)	1.00E+7
	Hole Thermal Velocity (cm/s)	1.00E+7
	Electron Mobility (cm^2/Vs)	1.00E+2
	Hole Mobility (cm^2/Vs)	2.50E+1
	Effective Mass of Electrons	2.00E-1
	Effective Mass of Holes	8.00E-1
	Shallow Uniform Donor Density N_A (cm^{-3})	1.00E+18

Table 4.7 Parameters of Defect 1 of CdS

CdS Defect 1	Parameter	Value
	Defect Type	Single Acceptor
	Capture Cross Section Electrons (cm^2)	1.00E-14
	Capture Cross Section Holes (cm^2)	1.00E-14
	Energetic Distribution	Single
	Reference for Defect Energy Level E_t	Above E_i
	Energy Level with Respect to Reference (eV)	0.0
	N_t total (cm^{-3})	1.0E+16

Table 4.8 Material Parameters for SnO₂ Layer

SnO ₂	Parameter	Value
	Thickness (μm)	.100
	Bandgap (eV)	3.6
	Electron Affinity (eV)	4.5
	Dielectric Permittivity (relative)	9
	CB Effective Density of States (cm ⁻³)	3.200E+18
	VB Effective Density of States (cm ⁻³)	2.500E+19
	Electron Thermal Velocity (cm/s)	1.00E+7
	Hole Thermal Velocity (cm/s)	1.00E+7
	Electron Mobility (cm ² /Vs)	1.00E+2
	Hole Mobility (cm ² /Vs)	2.50E+1
	Shallow Uniform Donor Density N _D (cm ³)	1.00E+18

Table 4.9 Parameters of Defect 1 of SnO₂

SnO ₂ Defect 1	Parameter	Value
	Defect Type	Neutral
	Capture Cross Section Electrons (cm ²)	1.00E-15
	Capture Cross Section Holes (cm ²)	1.00E-13
	Energetic Distribution	Gauß
	Reference for Defect Energy Level E _t	Above E _i
	Energy Level with Respect to Reference (eV)	0.0
	Characteristic Energy (eV)	.1
	N _t total (cm ⁻³)	1.00E+15
	N _t Peak (cm ⁻³ /eV)	5.642E+15

Table 4.10 Material Parameters of FTO

FTO	Parameter	Value
	Thickness (μm)	.300
	Bandgap (eV)	3.6
	Electron Affinity (eV)	4.8
	Dielectric Permittivity (relative)	9
	CB Effective Density of States (cm^{-3})	3.200E+18
	VB Effective Density of States (cm^{-3})	2.500E+19
	Electron Thermal Velocity (cm/s)	1.00E+7
	Hole Thermal Velocity (cm/s)	1.00E+7
	Electron Mobility (cm^2/Vs)	3.00E+1
	Hole Mobility (cm^2/Vs)	7.50E+0
	Shallow Uniform Donor Density N_D (cm^3)	5.00E+20

Table 4.11 Parameters of Defect 1 of FTO

FTO Defect 1	Parameter	Value
	Defect Type	Neutral
	Capture Cross Section Electrons (cm^2)	1.00E-15
	Capture Cross Section Holes (cm^2)	1.00E-12
	Energetic Distribution	Gauß
	Reference for Defect Energy Level E_t	Above E_i
	Energy Level with Respect to Reference (eV)	0.0
	Characteristic Energy (eV)	.1
	N_t total (cm^{-3})	1.00E+15
	N_t Peak (cm^{-3}/eV)	5.642E+15

Table 4.12 Material Parameters of Right (Front) Contact

	Parameter	Value
Front Contact	Thermionic Emission/Surface Recombination Velocity of:	
	Electrons	1.00E+7 cm/s
	Holes	1.00E+5 cm/s
	Calculate Flat Band Conditions Instead of Providing Φ_m	
	No Optical Filter	

4.2.2 Nanowire CdS/Nanowire Cu₂S Model

For the nanowire Cu₂S layer, it is assumed that the same amount of light is absorbed as is absorbed by planar Cu₂S. The reasoning behind this assumption is that optical scattering amongst the embedded nanowires will cause all photons to eventually pass through the Cu₂S and be absorbed normally if they have enough energy or not if they do not have enough energy.

For modeling Cu₂S nanowire with diameters below the Bohr Radius, the bandgap and absorption coefficients must be changed. The bandgap is determined by equation 2.15:

$$E_{g(QD)} = E_{g(bulk)} + \frac{\hbar^2}{2R^2} \left(\frac{1}{m_e} + \frac{1}{m_h} \right) \quad [2.15]$$

The change in absorption coefficient is modeled by moving the absorption edge with the bandgap. The absorption edge is defined as point when the material's absorption coefficient begins to rapidly increase, thus the material begins to absorb light. The absorption edge can be found with the equation:

$$\lambda_{abs\ edge}[in\ \mu m] = \frac{1.24\ \mu m/eV}{E_g} \quad [4.2]$$

For planar Cu₂S, the absorption edge is approximately 1025 nm. Shifting the entire absorption coefficient profile by moving the absorption edge is a good 1st order approximation of Cu₂S with a different bandgap. Figure 4.16 shows the shifted absorption coefficients for select bandgaps of Cu₂S.

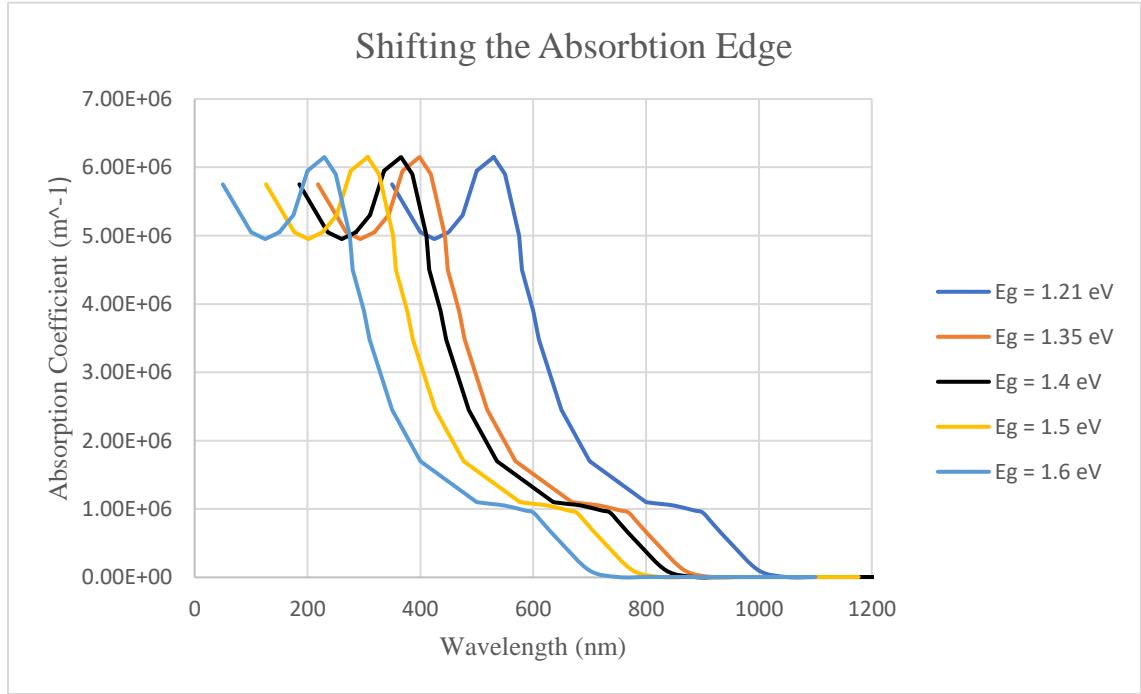


Figure 4.17: Absorption Coefficient Profile of Cu₂S with Different Bandgaps

The material parameters used to simulated the rest of the device are the same as those used for the nanowire CdS/planar Cu₂S device.

CHAPTER 5: RESULTS AND DISCUSSION

The following section describes the results of the simulations of nanowire CdS/planar Cu₂S and nanowire CdS/nanowire Cu₂S devices using SCAPS-1D.

5.1 Baseline Simulations

A planar CdS/planar Cu₂S device was first simulated using SCAPS-1D to discover the upper limits of performance without any added nanostructures. Traditionally, CdS/Cu₂S devices have been fabricated using CdS with thickness on the order of a few microns and Cu₂S with thickness close to 1 μ m [23, 35, 36]. These devices have been made with a maximum efficiency of 10.9%. The devices simulated instead use a 100 nm CdS layer.

5.1.1 Thickness Optimization

The first parameter that was explored was the thickness of the Cu₂S absorber layer. The starting thickness was 1 μ m with an external series resistance of 3 Ωcm^2 and shunt resistance of 3 $\text{k}\Omega\text{cm}^2$. It is assumed that series resistance is dominated by external effects, such as contact resistance and defects due to fabrication in the Cu₂S layer. Thickness was increased in increments of 1 μ m and the external series resistance increased by .1 Ωcm^2 per micron. The shallow acceptor concentration was set to $1.00\text{E}+17\text{ cm}^{-3}$. Figure 5.1 shows the results of changing the thickness of the Cu₂S on overall power conversion efficiency.

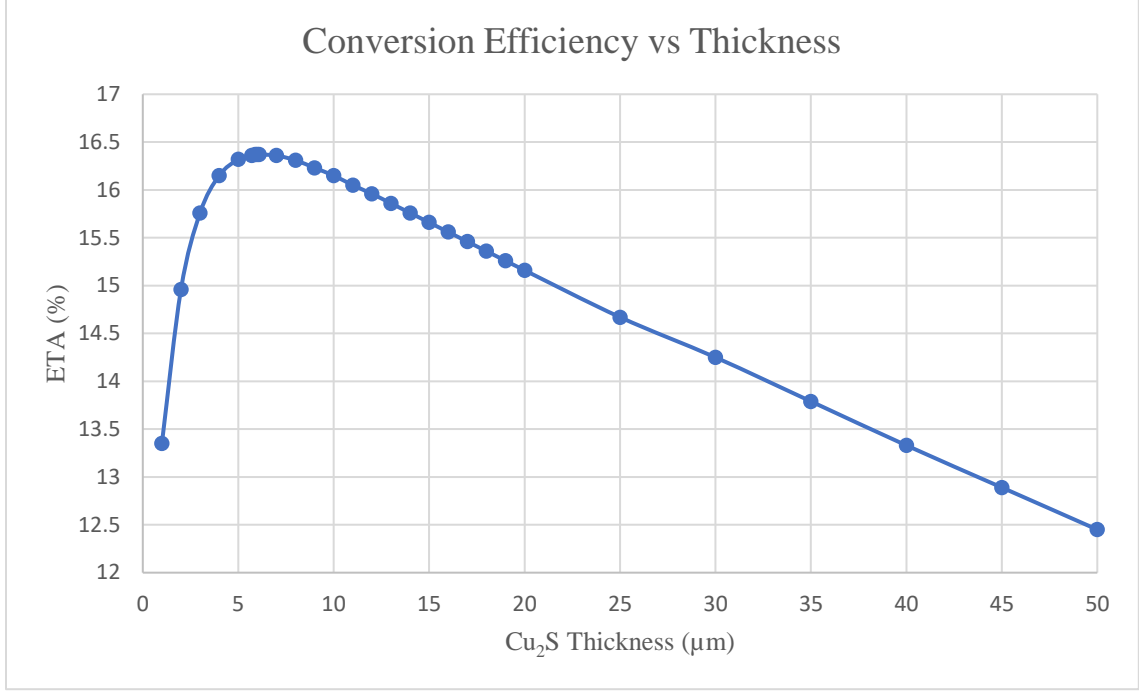


Figure 5.1: Thickness of Cu₂S Layer versus Power Conversion Efficiency (ETA)

The initial increase in efficiency can be attributed to increases in both short circuit current, J_{sc} , and open circuit voltage, V_{oc} . The subsequent decrease in efficiency can be attributed to a decrease in fill factor, FF, as well a slight decrease in J_{sc} . Equation 2.13 shows how the change in each of these parameters affects the overall efficiency:

$$ETA = \frac{P_{MPP}}{P_{solar}} = \frac{FF * I_{sc} * V_{oc}}{P_{solar}} \quad [2.13]$$

The changes in these parameters can be seen in figures 5.2-5.4.

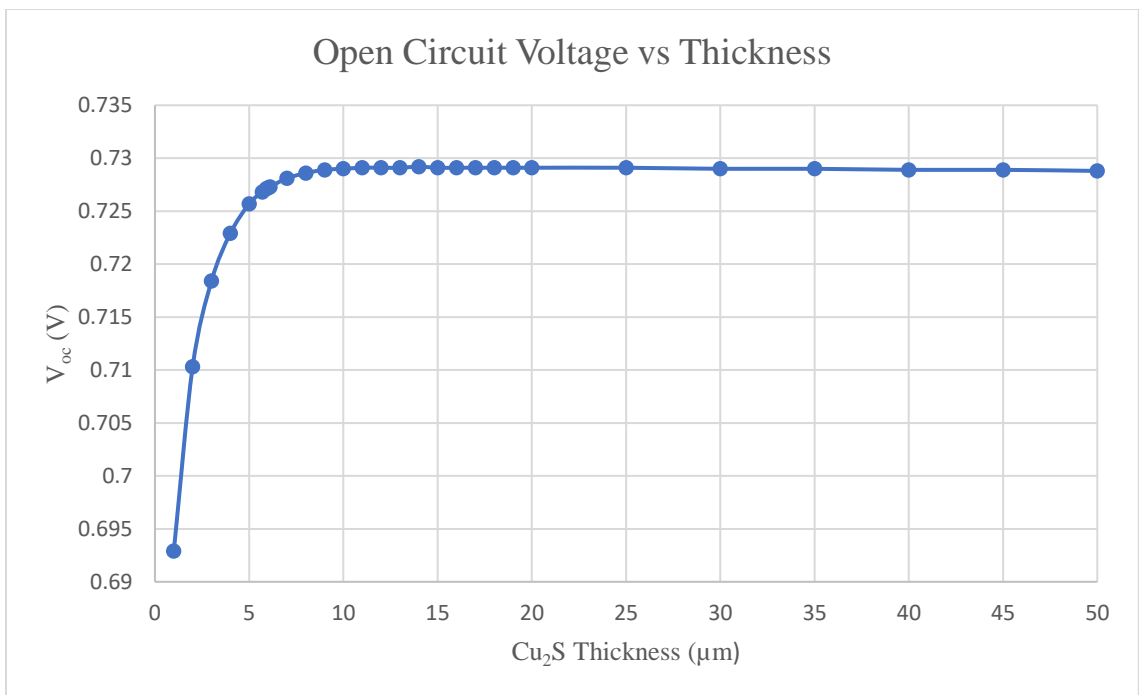


Figure 5.2: Thickness of Cu_2S Layer versus Open Circuit Voltage

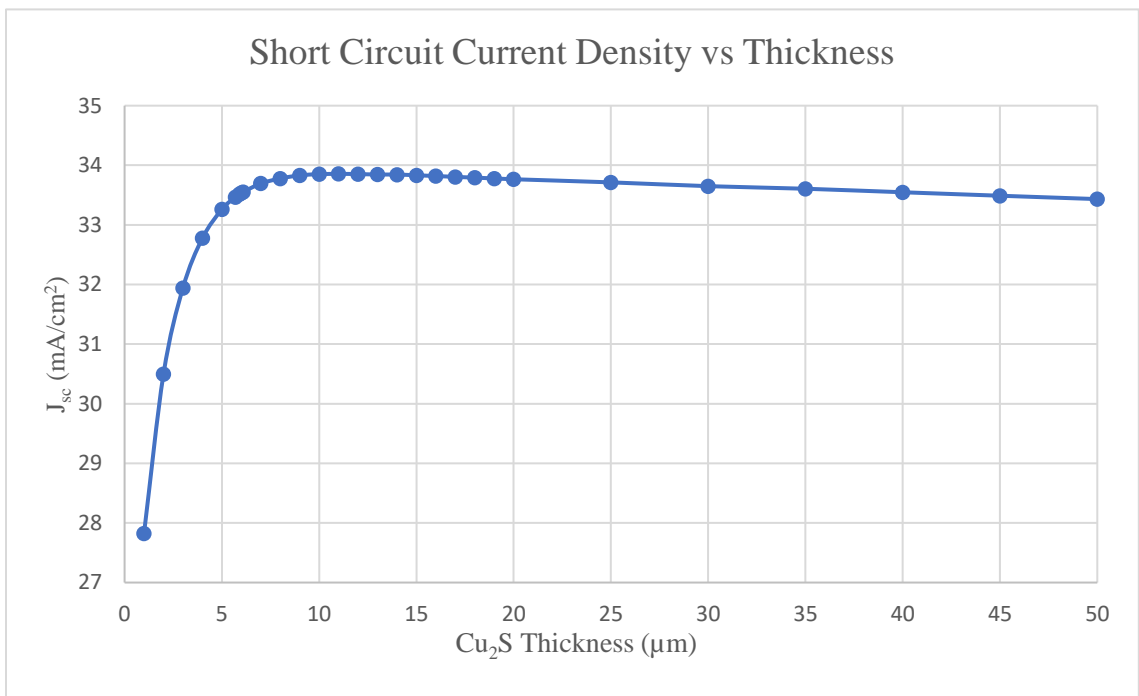


Figure 5.3: Thickness of Cu_2S Layer versus Short Circuit Current Density

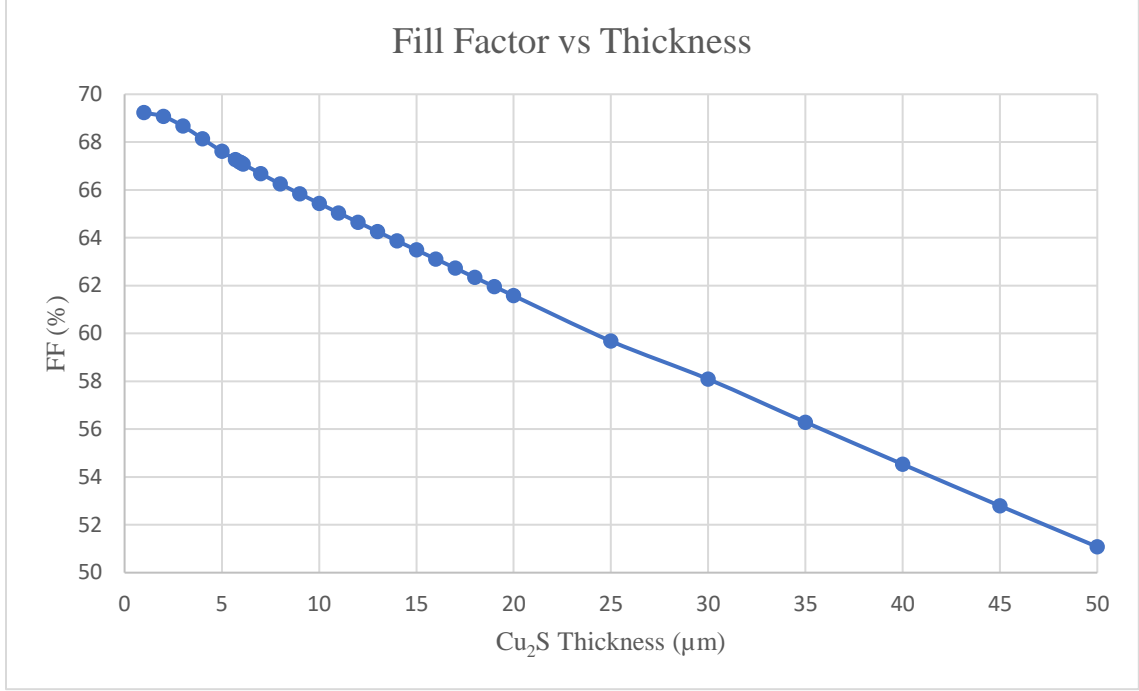


Figure 5.4: Thickness of Cu₂S Layer versus Fill Factor

The increase in short circuit current density is a result of an increase in light generated current density, J_L , in the Cu₂S region. Light generated current density can be approximated as:

$$J_L = q \int_0^W G(x)CP(x)dx \quad [5.1]$$

Where W is the layer thickness, G is the generation rate, and CP is the collection probability. $G(x)$ represents the incident photons in the layer and CP is how likely they are to be absorbed. Using this equation, it can be shown that increasing thickness allows for more incident photons to be absorbed until every photon that can be absorbed, has been absorbed. Figure 5.5 demonstrates this graphically.

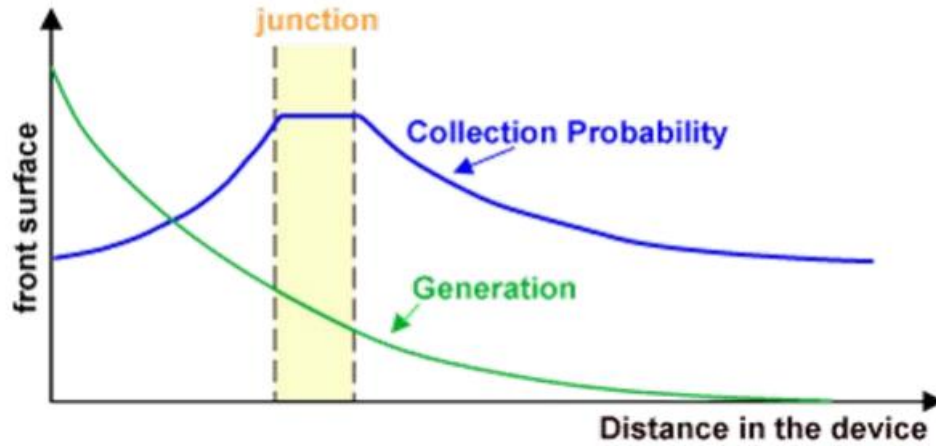


Figure 5.5: Collection Probability and Generation versus Thickness [37]

This increase in J_L is only valid for thicknesses less than the recombination length of electrons in Cu_2S . Once the thickness of Cu_2S exceeds this length, then electrons will recombine before they are able to reach the junction of the device. This is responsible for the decrease in J_{sc} after the initial increase. More photons are still absorbed, but the generated electrons recombine before they are able to be extracted.

The increase in J_{sc} directly leads to an increase in V_{oc} . This can be seen in

$$\text{equation 2.9: } V_{oc} = \frac{nkT}{q} \ln \left(\frac{J_{sc}}{J_0} + 1 \right) \quad [2.9]$$

In figure 5.4, FF can be seen to decrease linearly with increase in the thickness of copper sulfide. This is because the electrical resistance of the copper sulfide layer is directly proportional to its thickness and manifests itself as the additional internal series resistance in the current-voltage (I-V) characteristic of the solar cell. This makes the device less and less “ideal”. A perfectly ideal solar cell would have no external series resistance and infinite shunt resistance. The more “ideal” a solar cell is, the closer to rectangular shape its I-V characteristic would be. A perfectly rectangular I-V

characteristic has a fill factor of 100%. On the other hand, any additional internal series resistance results in an internal voltage drop loss, which makes the shape of the I-V characteristic more linear and less rectangular. Thus, increasing the copper sulfide layer thickness results in a lowering of the FF.

The optimal thickness of the Cu_2S layer was found to be $6\text{ }\mu\text{m}$ with a conversion efficiency of 16.37%. This is an increase of 5.47% over the highest efficiency achieved in traditional devices.

5.1.2 Doping Optimization

The shallow doping concentration, N_A , was then optimized with the Cu_2S thickness set to its optimal value of $6\text{ }\mu\text{m}$. The results of this optimization can be seen in figures 5.6-5.9.

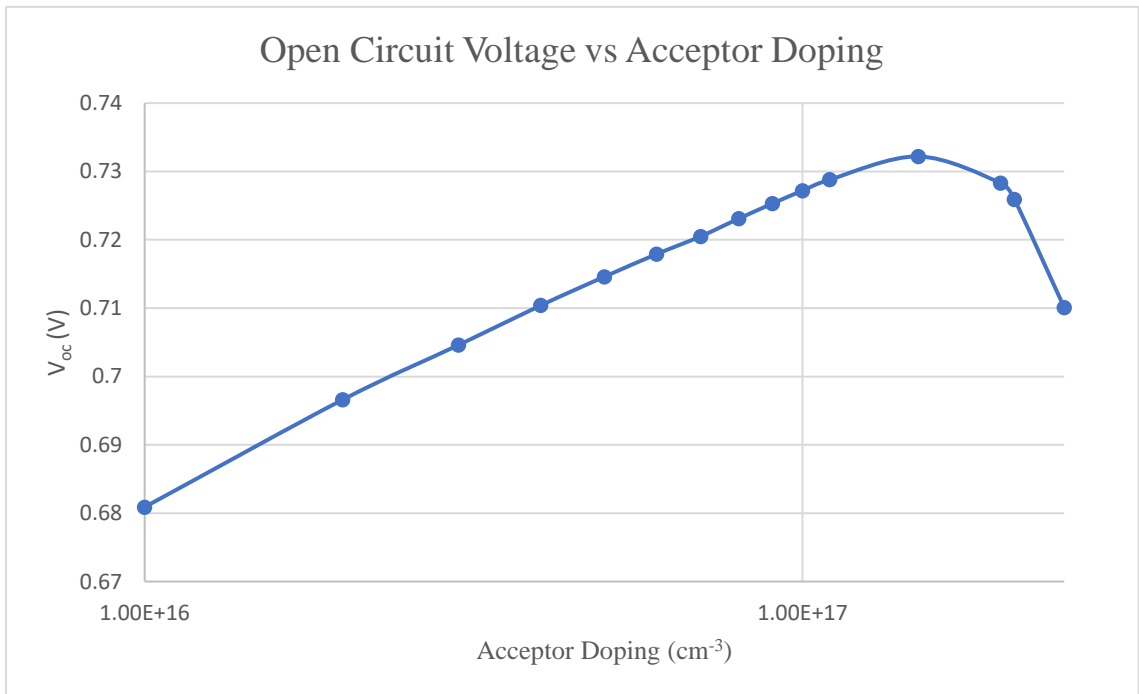


Figure 5.6: Open Circuit Voltage versus Acceptor Doping

Figure 5.6 shows that the V_{oc} increased with N_A up to $N_A = 1.5E+17 \text{ cm}^{-3}$, after which it began to rapidly drop off. This initial rise can be attributed to reductions in reverse saturation current density, J_0 , which decreases as a direct factor of N_A . This can be seen in equation 2.10:

$$J_0 = qN_cN_v \left(\frac{1}{N_A} \sqrt{\frac{D_n}{\tau_n}} + \frac{1}{N_D} \sqrt{\frac{D_p}{\tau_p}} \right) \exp\left(\frac{-E_g}{kT}\right) \quad [2.10]$$

This reduction factors into V_{oc} via equation 2.9:

$$V_{oc} = \frac{nkT}{q} \ln\left(\frac{J_{sc}}{J_0} + 1\right) \quad [2.9]$$

This results in the initial rise in V_{oc} that is observed. The decrease in V_{oc} after $N_A = 1.5E+17 \text{ cm}^{-3}$ can be attributed to the reduction in J_{sc} (see Fig. 5.7 below) becoming the dominant factor in the controlling of V_{oc} . In other words, increasing of N_A has two opposing effects on the solar cell performance. First, the Fermi level in copper sulfide moves closer to the valance band, which leads to increased junction barrier potential, V_{bi} , and a reduced reverse saturation current density, J_0 , as expressed quantitatively in Equation 2.10 above. This increases V_{oc} . Second, added dopants or defects, which are the source of N_A , facilitate recombination between the light generated electrons and the holes in copper sulfide. This loss of light generated electrons leads directly to a reduction in J_{sc} , with increasing N_A (Fig. 5.7). Next, reduction in J_{sc} leads to a logarithmic reduction in V_{oc} (Equation 2.9 above). The first effect is dominant below $N_A = 1.5E+17 \text{ cm}^{-3}$ in Fig. 5.6 while the second effect is dominant above $N_A = 1.5E+17 \text{ cm}^{-3}$.

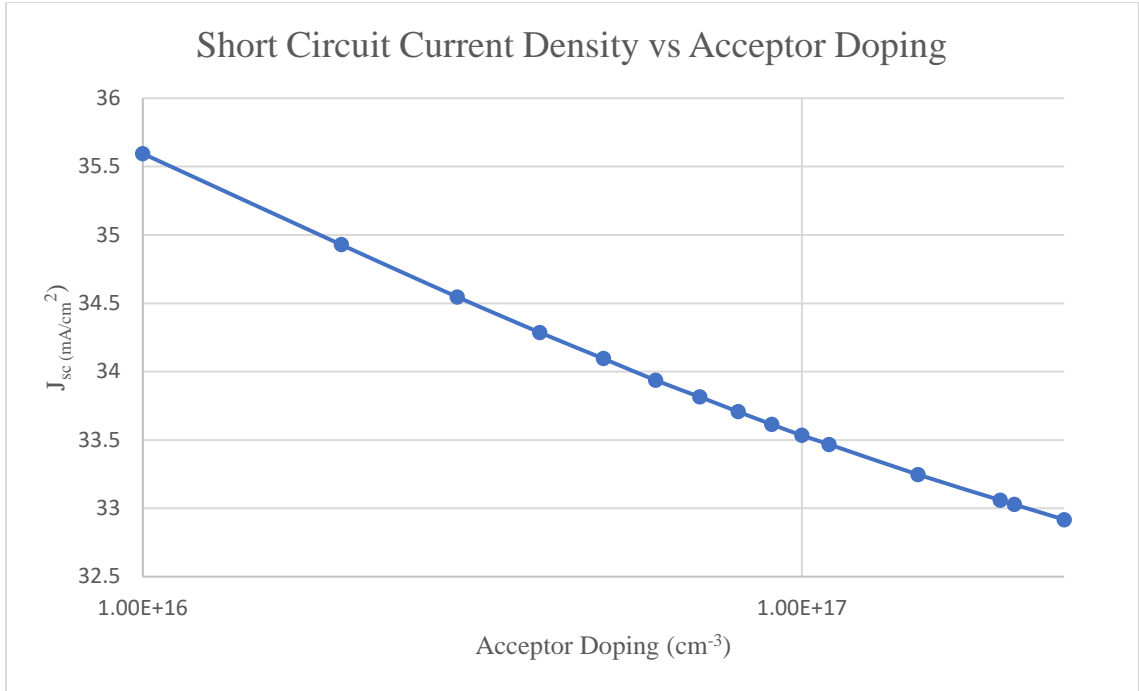


Figure 5.7: Short Circuit Current Density versus Acceptor Doping

Figure 5.7 shows that the short circuit current density decreases with increased N_A . As describes in the paragraph above, this behavior can be explained by recombination becoming more and more dominant with additional dopants acting as recombination sites throughout the Cu_2S . This prevents significant buildup of current and thus reduces J_{sc} .

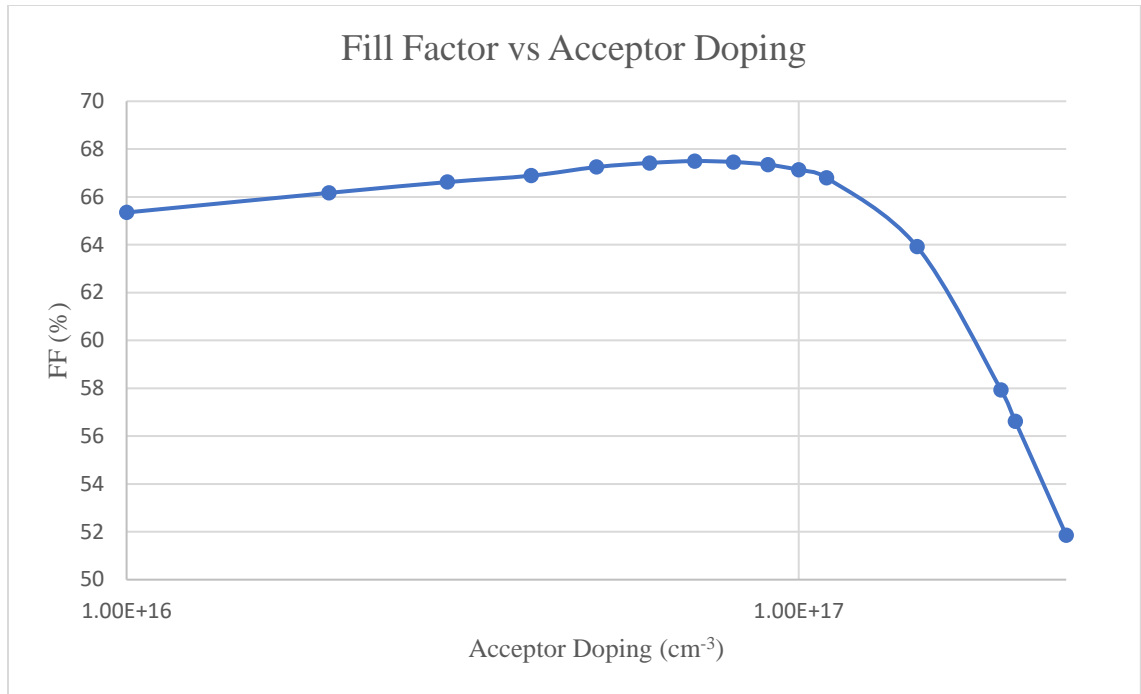


Figure 5.8: Fill Factor versus Acceptor Doping

Figure 5.8 shows the fill factor increasing for doping up to $7.00\text{E}+16\text{ cm}^{-3}$ and then rapidly dropping off. This drop off is due to recombination at doping cites becoming the dominant process for electrons in the Cu_2S layer. Fill factor is a quantitative measure of the shape of the I-V characteristic of a solar cell. More “ideal” a solar cell is, closer to rectangular shape its I-V characteristic would be. A perfectly rectangular I-V characteristic has a fill factor of 100%. In general, more the V_{oc} increases, more rectangular the I-V characteristic shape becomes, and FF is enhanced. In this sense, FF “tracks” V_{oc} . Explanation for the behavior seen in Fig. 5.8 is, therefore, same as the explanation of the behavior of fig. 5.6, described above.

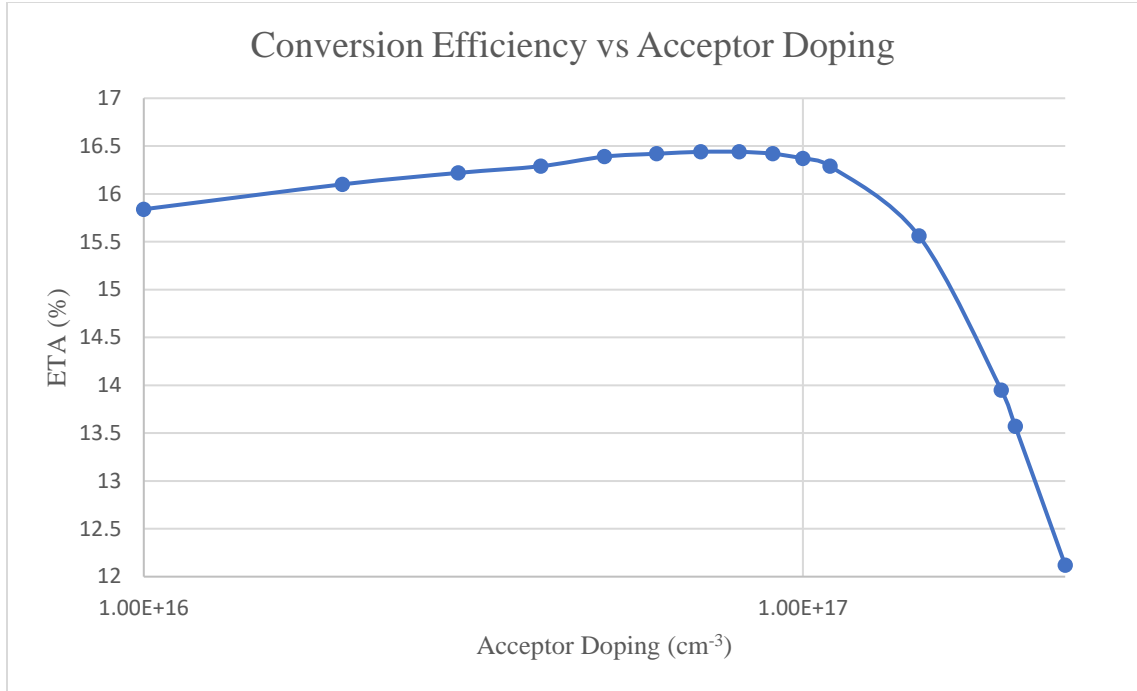


Figure 5.9: Conversion Efficiency versus Acceptor Doping

Figure 5.9 shows the conversion efficiency following the same path as FF, increasing for doping up to $7.00\text{E}+16 \text{ cm}^{-3}$ and then rapidly dropping off. This is due to recombination significantly reducing the short circuit current density as well as the open circuit voltage and fill factor dropping off. The optimal acceptor doping level was found to be $6\text{E}+16 \text{ cm}^{-3}$ with a conversion efficiency of 16.44%. This is an increase of 5.54% over the best efficiency value reported in the literature for these traditional planar devices.

5.2 Nanowire CdS/Planar Cu₂S Results

The effect of CdS nanowire coverage in a nanowire CdS/planar Cu₂S solar cell has been simulated using SCAPS-1D over a range of different doping levels. The model used for these simulations is described in section 4.2.1. The results can be seen in figures

5.10 – 5.17. CdS coverages have been split into two section, 100% - 40% and 35% - 1%.

This is due to SCAPS not being able to converge for heavily doped, high CdS coverage devices.

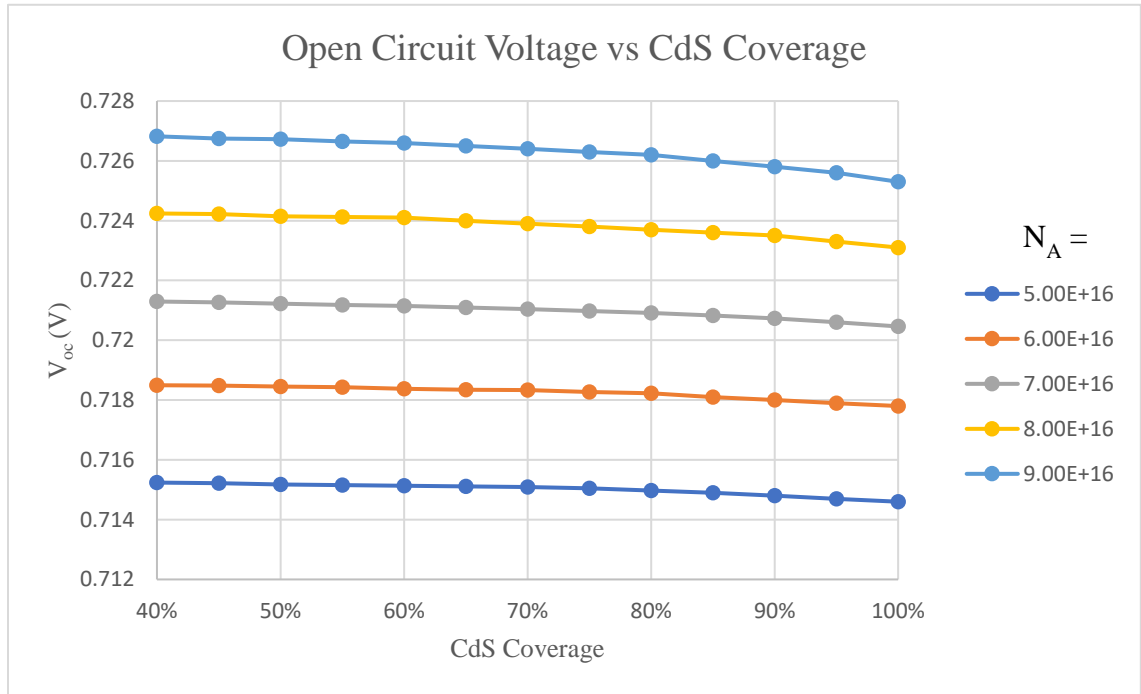


Figure 5.10: Effect of CdS Coverage 100% - 40% and Doping on Open Circuit Voltage

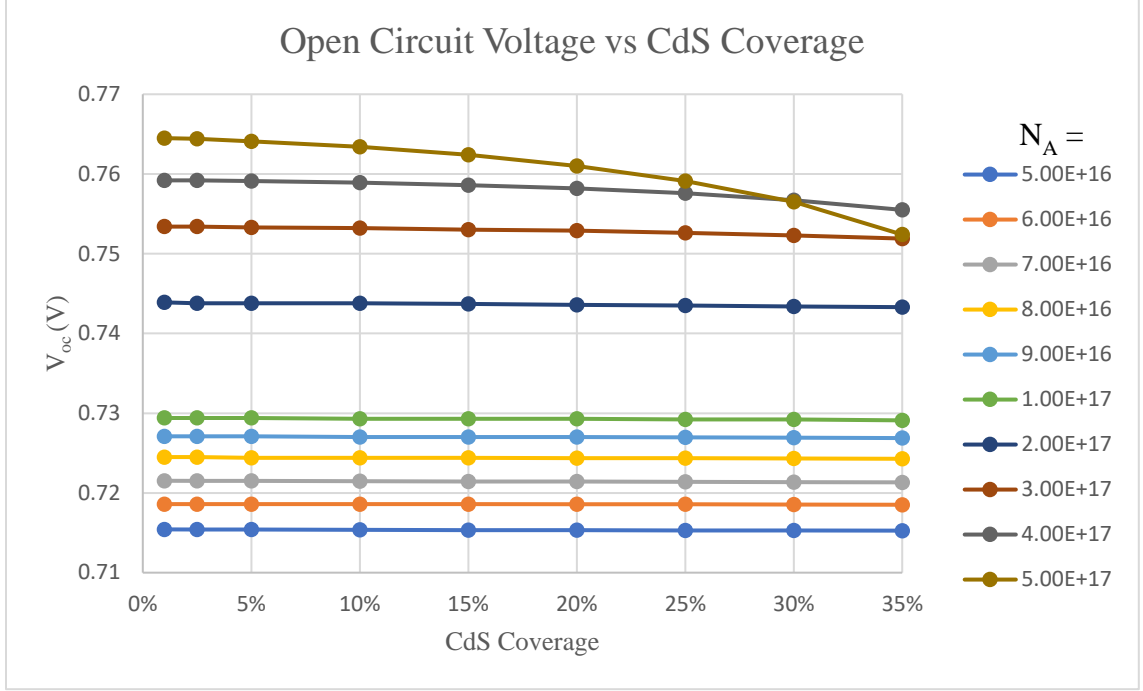


Figure 5.11: Effect of CdS Coverage 35% - 1% and Doping on Open Circuit Voltage

Figures 5.10 and 5.11 demonstrate that open circuit voltage increases as CdS coverage decreases. This is especially prevalent among the devices with $N_A > 1.00 \times 10^{17}$. The overall increase in V_{oc} can be attributed to the reduction in overall interface states at the junction. Interface states have been shown to be the dominant recombination mechanism at the junction for CdS/CdTe devices, and it is assumed that the same is true in CdS/Cu₂S devices [33]. Additionally, the presence of interface states has been shown to increase the reverse saturation current density, which in turn lowers the V_{oc} [38]. Thus, a reduction in interface states leads to a lower reverse saturation current density and a higher V_{oc} by equation 2.9:

$$V_{oc} = \frac{nkT}{q} \ln \left(\frac{J_{sc}}{J_0} + 1 \right) \quad [2.9]$$

The larger gain among the more heavily doped devices is due to further reduction of the reverse saturation current density. In equation 2.10, it can be seen that J_0 is inversely proportional to N_A , thus the benefit from decreased interface states is magnified in heavily doped devices. At lighter doping levels, the reduction in J_0 is minimized and so is the gain to V_{oc} .

$$J_0 = qN_C N_V \left(\frac{1}{N_A} \sqrt{\frac{D_n}{\tau_n}} + \frac{1}{N_D} \sqrt{\frac{D_p}{\tau_p}} \right) \exp \left(\frac{-E_g}{kT} \right) \quad [2.10]$$

The greatest V_{oc} obtained was 0.7645 V for a device an acceptor doping level of $5.00E+17 \text{ cm}^{-3}$.

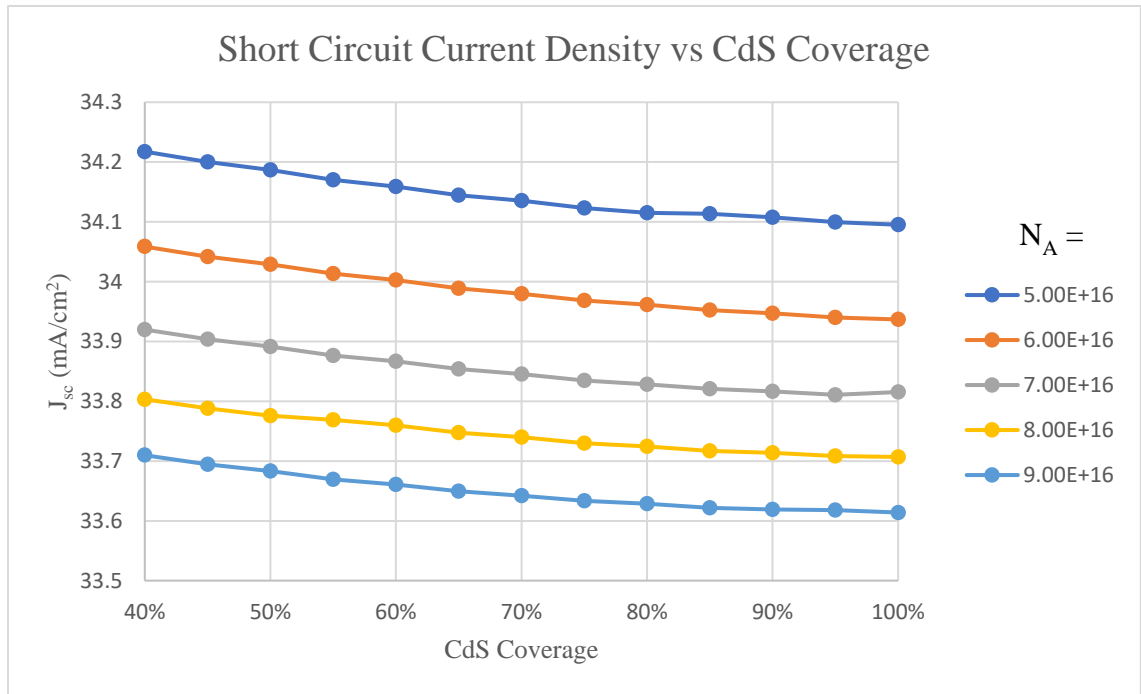


Figure 5.12: Effect of CdS Coverage 100% - 40% and Doping on Short Circuit Current Density

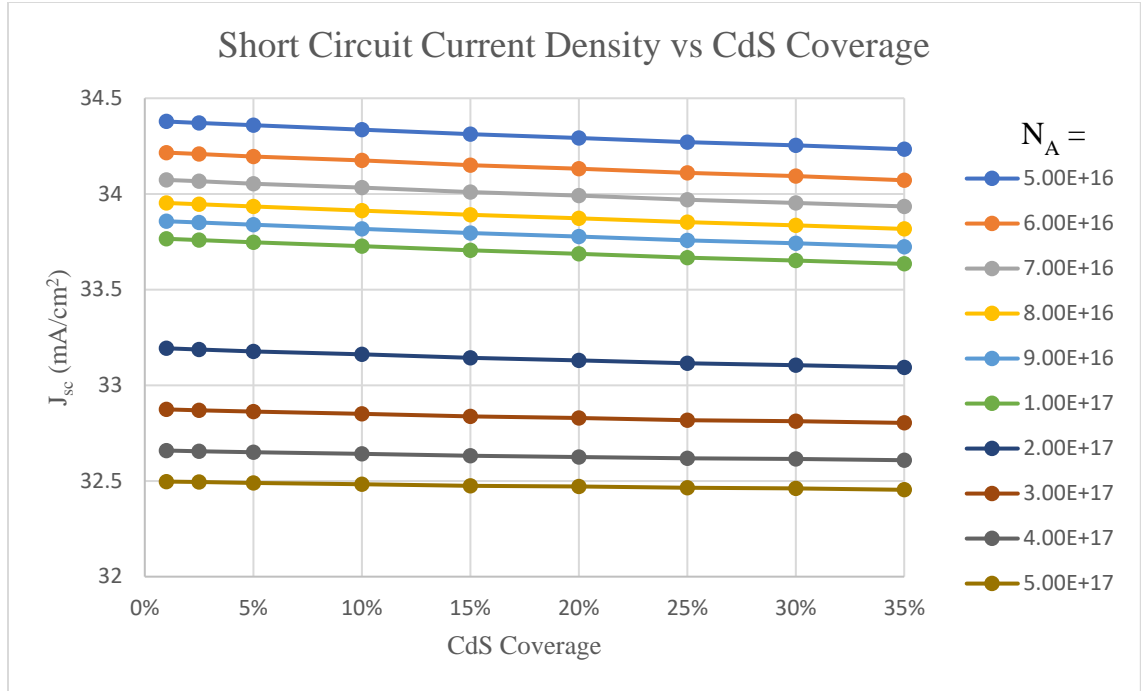


Figure 5.13: Effect of CdS Coverage 35% - 1% and Doping on Short Circuit Current Density

Figures 5.12 and 5.13 shows that as CdS coverage decreases, the short circuit current density increases. There are several factors at play that result in the increased short circuit current density. The first one being the increase in effective bandgap of CdS when deposited into nanowires. Planar CdS's bandgap of 2.42 eV allows for the absorption of sub 500nm photons in the CdS window layer where a large amount of recombination sites prevents the generated holes from contributing to the generated photocurrent. Nanowire CdS's effective bandgap of 3.5eV allows for photons of wavelength 500 nm to 345 nm to not be absorbed in the CdS window layer but instead in the Cu₂S absorber layer. This allows them to contribute to the overall generated photocurrent.

This increase in CdS's transmittivity at lower wavelengths is coupled with an overall increase in transmittivity due to the reduced surface area of nanowire structures. Only a percentage of Cu₂S is blocked by CdS with the rest being covered with a transparent layer of TiO₂, which allowed nearly all light to pass through without being absorbed. As CdS coverage decreases, more and more of the surface area is covered with TiO₂ which in turn allows more photons to reach the Cu₂S absorber layer where they contribute to the generated photo current.

At lighter levels of doping, the gain in J_{sc} is more prevalent with decreased CdS coverage. This is due to dopants acting as recombination centers. Thus, more heavily doped devices lose most of the current they gain from the increased transmission to recombination.

The greatest J_{sc} obtained was 34.378 mA/cm² with an acceptor doping level of 5.00E+16 cm⁻³.

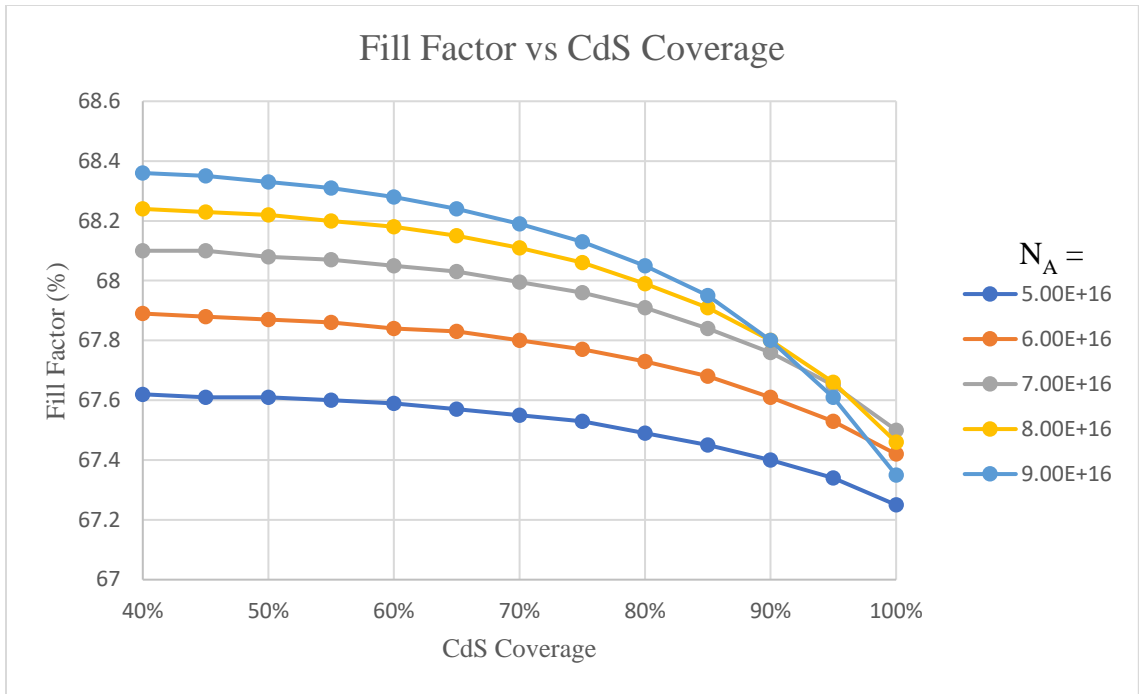


Figure 5.14: Effect of CdS Coverage 100% - 40% and Doping on Fill Factor

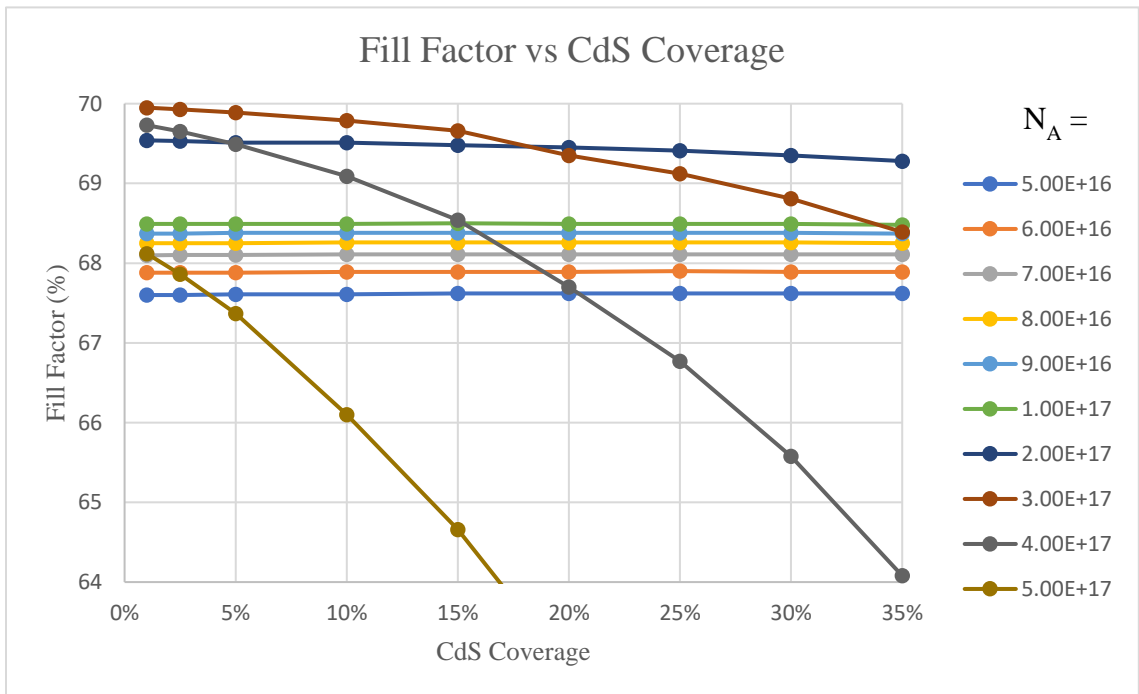


Figure 5.15: Effect of CdS Coverage 35% - 1% and Doping on Fill Factor

Figures 5.14 and 5.15 show that as CdS coverage decreases, the fill factor increases. When parasitic series and shunt resistant, R_s and R_{SH} , have negligible effects on device performance, then fill factor can be approximated by:

$$FF = \frac{\frac{qV_{oc}}{kT} - \ln\left(1.72 + \frac{qV_{oc}}{kT}\right)}{1 + \frac{qV_{oc}}{kT}} \quad [5.1]$$

This shows that the fill factor benefits from an increase in V_{oc} . At heavier doping levels, $N_A > 1.00E+17$, this effect is much more pronounced than it is for lighter doping levels. Devices with lighter doping levels have a higher bulk series resistance that counteracts the benefits gained from increased V_{oc} . Additionally, heavier doped devices demonstrated a greater gain in V_{oc} over the lightly doped devices, resulting in further enhancement of their fill factors.

The greatest FF obtained was 69.95% with an acceptor doping level of $3.00E+17 \text{ cm}^{-3}$.

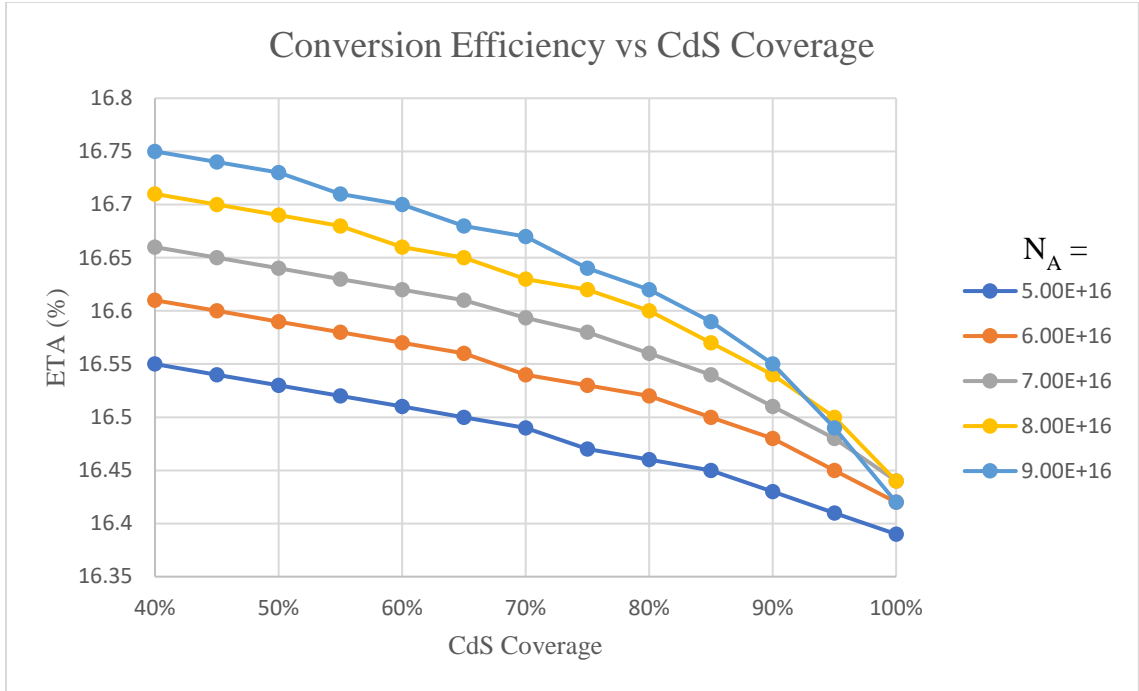


Figure 5.16: Effect of CdS Coverage 100% - 40% and Doping on Conversion Efficiency

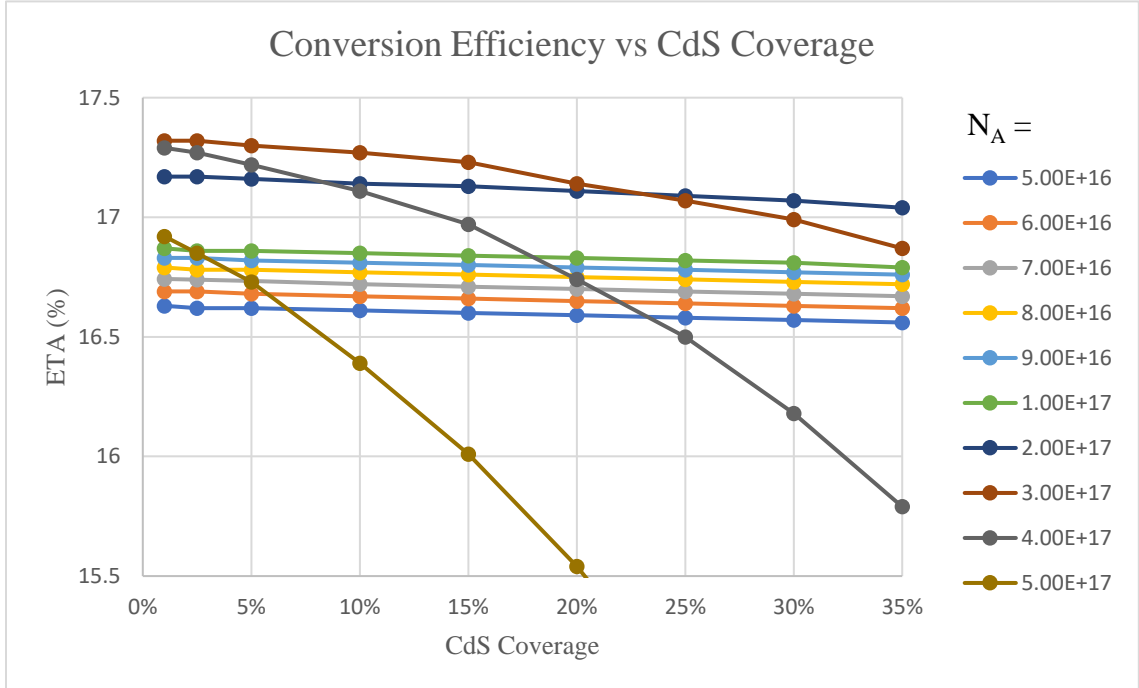


Figure 5.17: Effect of CdS Coverage 35% - 1% and Doping on Conversion Efficiency

Figures 5.16 and 5.17 show that as CdS coverage decreases, conversion efficiency increases. Efficiency is a function of V_{oc} , J_{sc} , and FF. As all these factors have been shown to increase as CdS coverage decrease, it is expected that the overall efficiency will increase as well. This effect is more pronounced in more heavily doped devices as it was for FF and V_{oc} . In lightly doped devices, the gains in V_{oc} and FF begin to saturate around 35% coverage of CdS. This leads to the efficiency saturating as well. The slight gains in efficiency when CdS coverage is reduced below 35% can be attributed to the continuous gain in J_{sc} that is present all the way to 1% CdS coverage.

The efficiency of devices with $N_A > 1.00E+17$ does not saturate until near 5% CdS coverage, with the highest dopings of $N_A = 5.00E+17$ and $4.00E+17$ not saturating at any point. This is due to the gains in V_{oc} and FF that are prevalent in heavily doped devices.

The greatest conversion efficiency obtained was 17.32% with an acceptor doping level of $3.00E+17 \text{ cm}^{-3}$. This is a gain of 6.72% over traditionally made CdS/Cu₂S solar cells and a gain of .88% over an optimized planar CdS/planar Cu₂S solar cell. This shows that nanostructures can be used to substantially improve the performance of CdS/Cu₂S solar cells.

5.3 Nanowire CdS/Nanowire Cu₂S Results

The effect of depositing Cu₂S into nanotubes of different diameters with a range of different levels of doping has been simulate using SCAPS-1D. The model used for these simulation is described in section 4.2.2.

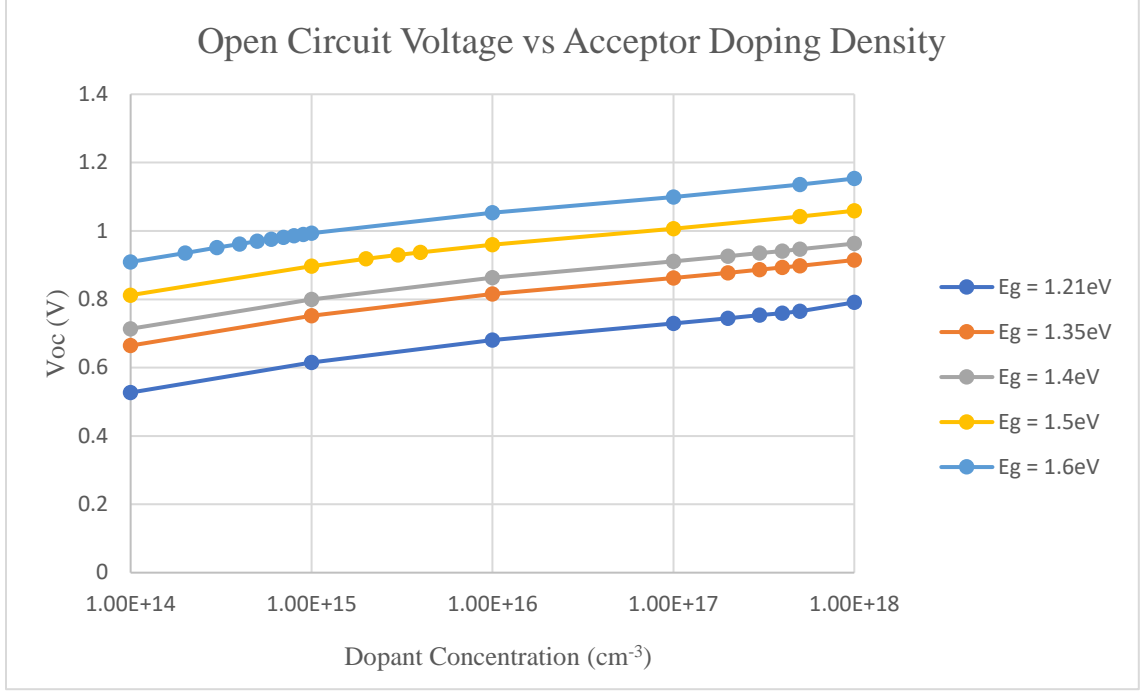


Figure 5.18: Effect of E_g and Doping on Open Circuit Voltage

Figure 5.18 shows that as the effective bandgap of Cu_2S absorber layer increased, so does the open circuit voltage. This effect is due to E_g reducing the reverse saturation current, J_0 , as it increases. This results in a direct increase of V_{oc} .

$$J_0 = qN_cN_v \left(\frac{1}{N_A} \sqrt{\frac{D_n}{\tau_n}} + \frac{1}{N_D} \sqrt{\frac{D_p}{\tau_p}} \right) \exp \left(\frac{-E_g}{kT} \right) \quad [2.10]$$

Increasing acceptor doping, N_A , is also observed to increase the V_{oc} . This is also an effect of reducing J_0 . This is due to J_0 being inversely proportional to N_A . Additionally, the built in voltage, V_{bi} , will also increase with the bandgap.

The greatest V_{oc} achieved was 1.1533 V with an acceptor doping density of $1.00\text{E}+18 \text{ cm}^{-3}$ and bandgap of 1.6eV.

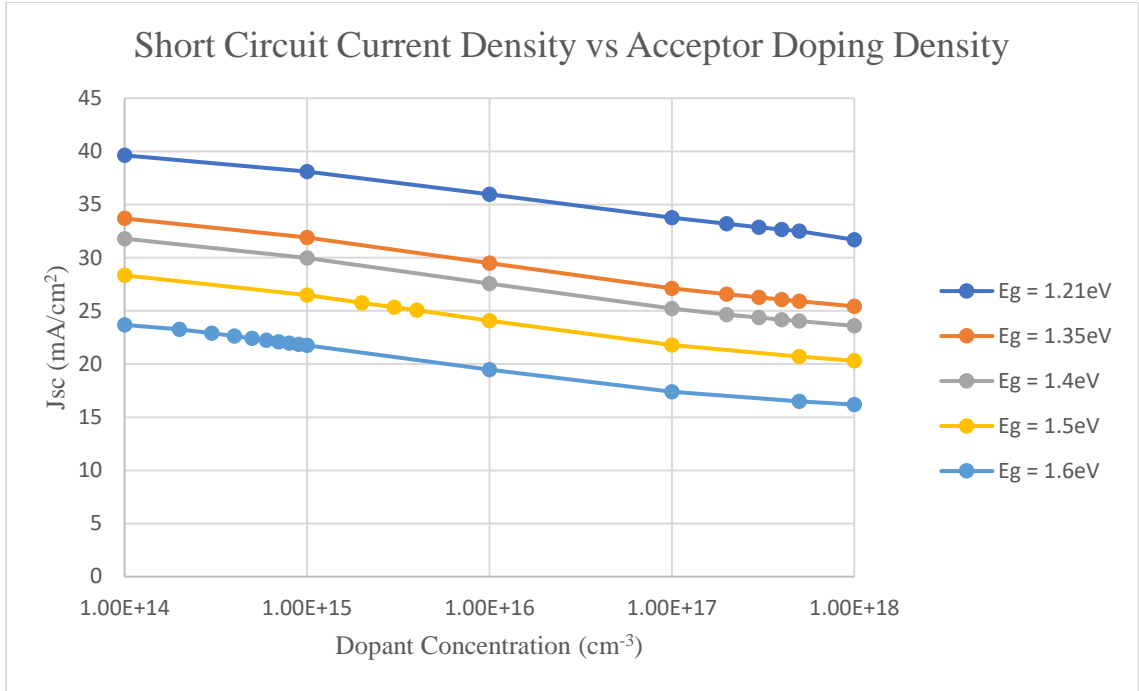


Figure 5.19: Effect of E_g and Doping on Short Circuit Current Density

Figure 5.19 shows that as both the acceptor doping level and effective bandgap increases, the short circuit current density decreases. This is due to two distinct effects. It has been previously mentioned that increasing N_A results in an increase of recombination due to dopants acting as recombination sites. This effect results in the observed decrease in J_{sc} .

The changing bandgap affects J_{sc} by reducing the quantity of high wavelengths photons that can be absorbed. As E_g increases, photons require a greater amount of energy to be absorbed. Therefore, with each step up in E_g , some photons, which would have been absorbed by a lower E_g material and contributed to the generated photocurrent are no longer able to do so. The greatest J_{sc} achieved was $39.632411 \text{ mA}/\text{cm}^2$ with a doping level of $1.00\text{E}+14 \text{ cm}^{-3}$ and bandgap of 1.21 eV

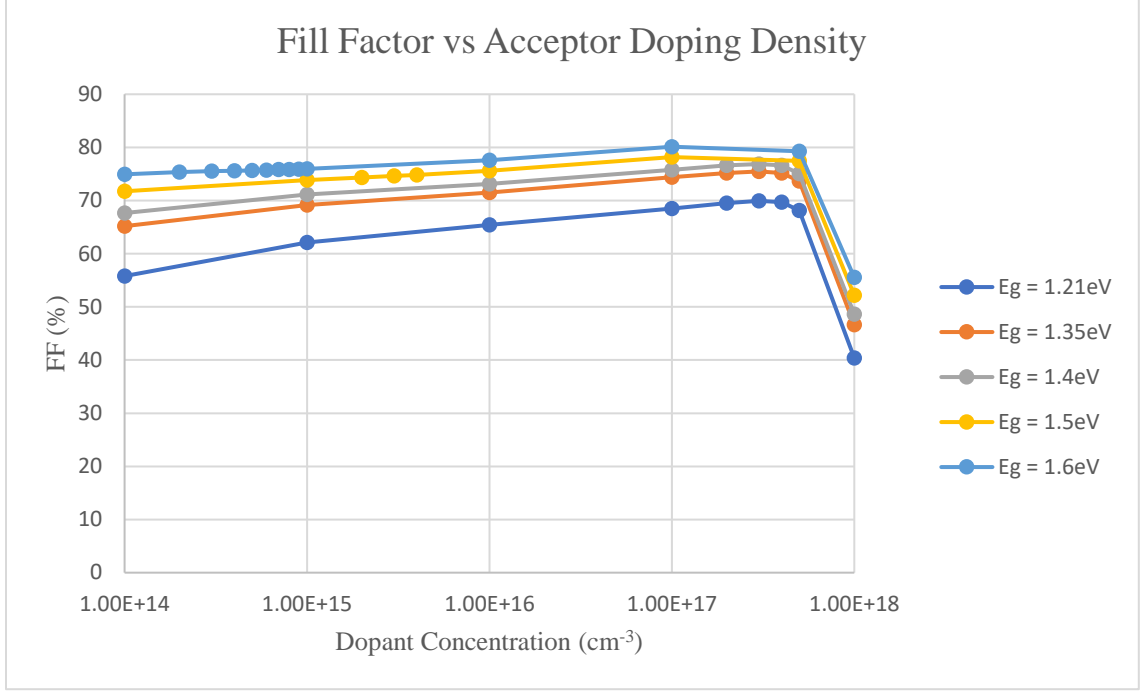


Figure 5.20: Effect of E_g and Doping on Fill Factor

Figure 5.20 shows that as the acceptor doping increases, so does the fill factor up to a point. At doping levels greater than $5.00\text{E}+17$, the fill factor begins to drop. The initial rise in fill factor is due to enhancement of V_{oc} by reduction of J_0 , but this process is overshadowed when doping becomes so high that the reduction in J_{sc} and V_{oc} (and hence FF), caused by the excessive recombination facilitated by N_A becomes the dominant factor. The initial effect of V_{oc} on FF is described by the equation:

$$FF = \frac{\frac{qV_{oc}}{kT} - \ln\left(0.72 + \frac{qV_{oc}}{kT}\right)}{1 + \frac{qV_{oc}}{kT}} \quad [5.1]$$

FF is also observed to increase with E_g . This is also due to enhancement of V_{oc} . This effect does not saturate due to it not creating any additional defects as it increases.

The greatest FF obtained was 80.13% with an acceptor doping level of $1.00\text{E}+17$ cm^{-3} and bandgap of 1.6 eV.

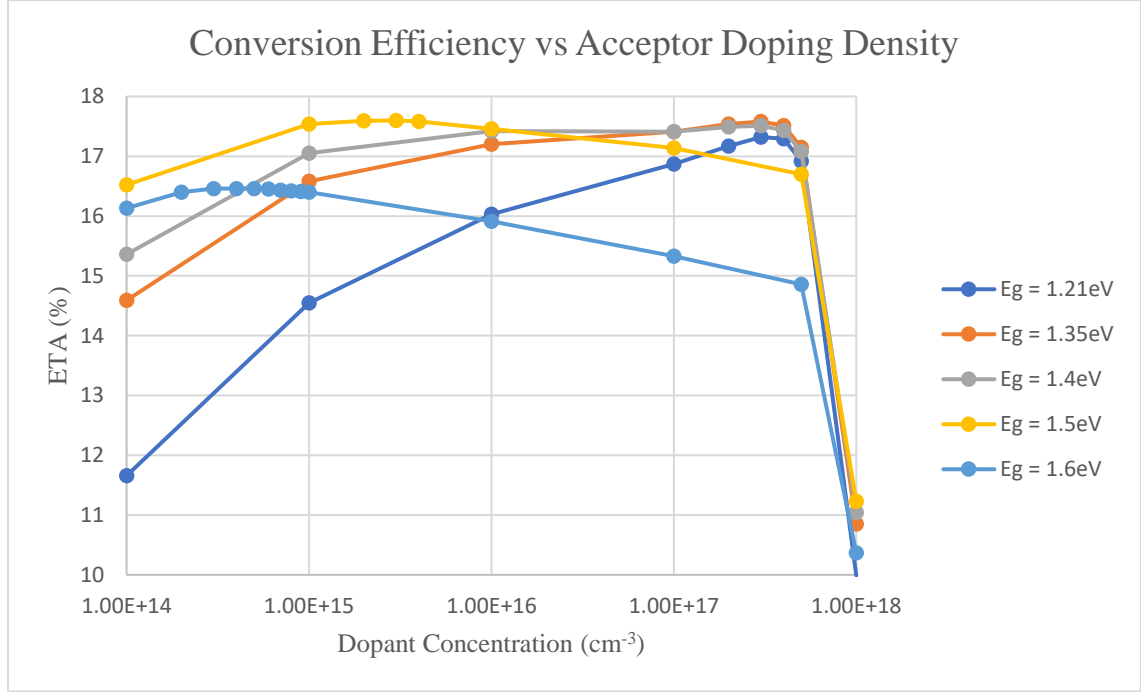


Figure 5.21: Effect of E_g and Doping on Conversion Efficiency

Figure 5.21 shows the various effects of acceptor doping and bandgap on conversion efficiency. Various effects dominate at different doping levels and bandgaps. At lower bandgaps, efficiency is observed to increase with doping levels up to approximately $5.00\text{E}+17$ cm^{-3} , at which point it rapidly drops off. The initial rise can be attributed to the gains in V_{oc} and FF due to the lowering of J_0 . The sudden decrease occurs when dopants that act as recombination sites have high enough concentration to become the dominant process for electrons in the Cu_2S absorber layer.

Higher bandgaps display the same behavior but at lower doping levels. This is due to there being less overall light-generated carriers. With less photons being absorbed, it takes a lower level of doping for recombination to become the dominant process.

The greatest efficiency obtained was 17.60% with an acceptor doping level of $3.00\text{E}+15\text{ cm}^{-3}$ and bandgap of 1.5 eV. This is an increase of 7% over traditional devices, 1.16% over optimized planar devices, and .28% over nanowire CdS devices.

From these results, it can be concluded that there is a benefit to developing a nanowire CdS/nanowire Cu₂S device over a traditional planar device or a nanowire CdS/planar Cu₂S device.

6. CONCLUSION

Based on various simulations done using SCAPS1-D on nanostructured CdS/Cu₂S solar cells, several major benefits to each design can be concluded.

Nanowire CdS/Planar Cu₂S:

1. A reduction of interface states between CdS and Cu₂S due to the reduced surface area. This leads to a gain in open circuit voltage by reducing the effective reverse saturation current. This, in turn, leads to a gain in fill factor.
2. An increase in transmission of photons through the window CdS layer. This is due to the dual effects of replacing most of the non-transmissive CdS with highly a transparent TiO₂ template and the increased effective bandgap of CdS when it is placed into nanotubes. These additional photons are then available to be absorbed by Cu₂S where they are better able to contribute to the generated photocurrent and slightly boost the open circuit voltage as well.

These benefits work together to increase efficiency by 6.72% compared to traditional devices and .88% compared to an optimized device. This enhancement of efficiency is obtained with a CdS coverage of 1%, acceptor doping level of $3.00\text{E}+17\text{ cm}^{-3}$, and thickness of 6 μm .

Nanowire CdS/Nanowire Cu₂S:

1. The same benefits to open circuit voltage, short circuit current, fill factor, and efficiency due to reduced CdS coverage are obtained in this device design as well.

2. The bandgap of Cu₂S can be tuned to more closely match up with the theoretical maximum efficiency predicted by the Shockley-Queisser Limit. This bandgap adjustment lead to the optimal absorption of the most photons possible.

With the assumption that scattering allows nanowires of Cu₂S to absorb all the incident photons, this devices structure further enhances the power conversion efficiency to reach a maximum value of 17.60% for Cu₂S with an effective bandgap of 1.5eV, CdS coverage of 1%, acceptor doping level of $3.00\text{E}+15\text{ cm}^{-3}$, and copper sulfide absorber thickness of 6 μm . This is an improvement of 7% over traditional planar devices, 1.16% over optimized planar devices, and 0.28% over nanowire CdS/planar Cu₂S devices.

CdS/Cu₂S, if it can be fabricated such that the Cu₂S remains stable, shows much promise as a thin film nanostructured device due to its competitive efficiency, affordability of materials, and lack of toxicity.

REFERENCES

- [1] A. E. Becquerel, “Memoire sur les Effects d’Electriques Produits Sous l’Influence des Rayons Solaires,” *Comptes Rendus de l’Academie des Sciences*, Vol. 9, 1839, pp. 561-567.
- [2] Nokia Bell Labs, 1941. *Light-Sensitive Electric Device*. US2402662.
- [3] D. M. Chapin, C.S.F., and G. L. Pearson, A New Silicon p-n Junction Photocell for Converting Solar Radiation into Electrical Power. *J. Appl. Phys.*, 1954. 25: p. 676
- [4] J. F. Geisz *et al.*, "Building a Six-Junction Inverted Metamorphic Concentrator Solar Cell," in *IEEE Journal of Photovoltaics*, vol. 8, no. 2, pp. 626-632, March 2018.
- [5] R. Paschotta, article on '[band gap](#)' in the [RP Photonics Encyclopedia](#), accessed on 2020-04-08
- [6] R. C. Neville, “CHAPTER V - BASIC THEORETICAL PERFORMANCE,” in *Solar Energy Conversion*, Elsevier Science, 1995, pp. 155–195.
- [7] By Squirmymcphree - Own work, CC BY-SA 3.0, <https://commons.wikimedia.org/w/index.php>
- [8] Electrical4U, “Characteristics of a Solar Cell and Parameters of a Solar Cell,” *Electrical4U*, 15-May-2018. [Online]. Available: <https://www.electrical4u.com/characteristics-and-parameters-of-a-solar-cell/>. [Accessed: 06-Apr-2020].
- [9] A. Rothwarf, “The CdS/Cu₂S solar cell: Basic operation and anomalous effects,” *Solar Cells*, vol. 2, no. 2, pp. 115–140, Mar. 1980.

- [10] Y. Zhao, H. Pan, Y. Lou, X. Qiu, J. Zhu, and C. Burda, “Plasmonic Cu_{2-x}S Nanocrystals: Optical and Structural Properties of Copper-Deficient Copper(I) Sulfides.,” *ChemInform*, vol. 40, no. 28, Mar. 2009.
- [11] N. Larsson, “Optical and Structural Properties of Cu_xS Quantum Dots Concerning H₂O/Ethanol Solvent Ratio.,” Master of Science, Materials Engineering, KTH Royal Institute of Technology, Stockholm, Sweden, 2013,[Online]. Available: <http://www.diva-portal.org/smash/record.jsf?pid=diva2%3A756167&dswid=1217>. [Accessed on 06-Apr-2020].
- [12] W. Shockley and H. J. Queisser, “Detailed Balance Limit of Efficiency of p-n Junction Solar Cells,” *Journal of Applied Physics*, vol. 32, no. 3, pp. 510–519, Mar. 1961.
- [13] S. Rühle, “Tabulated values of the Shockley–Queisser limit for single junction solar cells,” *Solar Energy*, vol. 130, pp. 139–147, Jun. 2016.
- [14] D. Kumar, “Investigation of Host Nanotube Parameter for Enhancing Performance of Nanostructured CdS-CdTe Solar Cells”, Master of Science, Electrical Engineering, University of Kentucky, Lexington, Ky, 2020
- [15] Tighineanu, A.; Ruff, T.; Albu, S.; Hahn, R.; Schmuki, P. Conductivity of TiO₂ nanotubes: Influence of annealing time and temperature. *Chem. Phys. Lett.* 2010, 494, 260–263.
- [16] H. I. Salim, O. I. Olusola, A. A. Ojo, K. A. Urasov, M. B. Dergacheva, and I. M. Dharmadasa, “Electrodeposition and characterisation of CdS thin films using thiourea

precursor for application in solar cells,” *Journal of Materials Science: Materials in Electronics*, vol. 27, no. 7, pp. 6786–6799, May 2016.

[17] O. K. Echendu, U. S. Mbamara, K. B. Okeoma, C. Iroegbu, C. A. Madu, I. C. Ndukwe, and I. M. Dharmadasa, “Effects of deposition time and post-deposition annealing on the physical and chemical properties of electrodeposited CdS thin films for solar cell application,” *Journal of Materials Science: Materials in Electronics*, vol. 27, no. 10, pp. 10180–10191, Apr. 2016.

[18] F. B. Dejene, I. M. Dharmadasa, and F. C. Eze, “Characteristics of Nanocrystallite-CdS Produced by Low-Cost Electrochemical Technique for Thin Film Photovoltaic Application: The Influence of Deposition Voltage,” *International Journal of Photoenergy*, Nov. 2017.

[19] Kewanee Oil Company, 1968. *Formation of Barrier Layers in Cadmium Sulfide Solar Cells*. US3374108.

[20] Kewanee Oil Company, 1969. *Method of Producing Polycrystalline Photovoltaic Cells*. US3480473

[21] J. J. Loferski, “Investigation of thin film solar cells based on Cu/sub 2/S and certain ternary compounds,” 1977.

[22] K. W. Boer, “Heat Treatment of Dip-Formed Cuprous Sulfide Films.”

[23] A. Ashour, “The physical characteristics of Cu₂S/CdS thin-film solar cell,” *JOURNAL OF OPTOELECTRONICS AND ADVANCED MATERIALS*, vol. 8, no. 4, pp. 1447–1451, Aug. 2006.

[24] SCAPS Manual

<https://users.elis.ugent.be/ELISgroups/solar/projects/scaps/SCAPS%20manual%20most%20recent.pdf>

[25] S. Bansal and P. Aryal, "Evaluation of new materials for electron and hole transport layers in perovskite-based solar cells through SCAPS-1D simulations," 2016 IEEE 43rd Photovoltaic Specialists Conference (PVSC), Portland, OR, 2016, pp. 0747-0750.

[26] M. N. Harif, S. F. Abdullah, A. W. Mahmood Zuhdi, F. Za'abar, M. S. Bahrudin and A. H. Hasani, "Simulation Analysis on CIGS Solar Cell on Different Absorber Layer Thickness Subject to Temperature Change Using SCAPS 1-D Software," 2018 IEEE International Conference on Semiconductor Electronics (ICSE), Kuala Lumpur, 2018, pp. 201-204.

[27] F. D. Silva and D. N. Micha, "High-Efficiency GaAs Solar Cell Optimization by Theoretical Simulation," 2019 34th Symposium on Microelectronics Technology and Devices (SBMicro), Sao Paulo, Brazil, 2019, pp. 1-4.

[28] M. Olopade, A. Adewoyin, M. Chendo and A. Bolaji, "The Study of Some Materials as Buffer Layer in Copper Antimony Sulphide (CUSbS₂) Solar Cell Using SCAPS 1-D," 2017 IEEE 44th Photovoltaic Specialist Conference (PVSC), Washington, DC, 2017, pp. 2381-2384.

[29] "Standard Solar Spectra," *PVEducation*, 2019. [Online]. Available: <https://www.pveducation.org/pvcdrom/appendices/standard-solar-spectra>. [Accessed: 13-Apr-2020].

- [30] H.J. Pauwels, G. Vanhoutte, Influence of interface states and energy barriers on efficiency of heterojunction solar-cells, *J. Phys. D-Appl. Phys.*, 11 (1978) 649-667.
- [31] A. Niemegeers, M. Burgelman, and A. D. Vos, "On the CdS/CuInSe₂ conduction band discontinuity," *Applied Physics Letters*, vol. 67, no. 6, pp. 843–845, May 1995.
- [32] Dang, H., Singh, V. P., Guduru, S., Hastings, J. T. "Embedded nanowire window layers for enhanced quantum efficiency in window-absorber type solar cells like CdS/CdTe". *Solar Energy Materials and Solar Cells* 2016, 144, 641-651.
- [33] Dang, H., Singh, V. P., Guduru, S., Bowie, J., Cambron, D. "Electrooptical characterization of n-CdS nanowires/p-CdTe heterojunction solar cell devices". In 2014 IEEE 40th Photovoltaic Specialist Conference (PVSC); IEEE, 2014; pp 1601-1606.
- [34] H. Dang, E. Ososanya, N. Zhang and V. Singh, "Numerical modeling and simulation of stable nanowire CdS-CdTe solar cells," 2017 IEEE 17th International Conference on Nanotechnology (IEEE-NANO), Pittsburgh, PA, 2017, pp. 171-176.
- [35] W. F. Mohammed and M. Al-Tikriti, "Novel electronic approach for efficient energy harvesting from Cu₂S/CdS solar cell," 2015 IEEE 12th International Multi-Conference on Systems, Signals & Devices (SSD15), Mahdia, 2015, pp. 1-8.
- [36] J. Bragagnolo, A. Barnett, J. Phillips, R. Hall, A. Rothwarf, and J. Meakin, "The design and fabrication of thin-film CdS/Cu₂S cells of 9.15-percent conversion efficiency," *IEEE Transactions on Electron Devices*, vol. 27, no. 4, pp. 645–651, 1980.
- [37] Y. Baghzouz, Class Lecture, Topic: " 4.1 SOLAR CELL OPERATION.", College of Engineering and Science, University of Nevada, Las Vegas

- [38] H.M. Dang, Vijay Singh, Suresh Rajaputra, Sai Guduru, Sai Guduru, Jianhao Chen, Bhavananda Nadimpally, "Cadmium sulfide nanowire arrays for window layer applications in solar cells", *Solar Energy Materials and Solar Cells*, 26, 184-191, 2014.
- [39] A.W. Czandema, C.N.R. Rao, J.M. Honig, *Trans. Faraday Soc.* 54 (1958) 1069.
- [40] J. Tsao , N. Lewis , G. Crabtree , *Solar FAQs* , US Department of Energy , USA 2006
- [41] BP, *BP Statistical Review of World Energy 2019 68th Edition* . London, UK: BP, 2019.
- [42] M. M. Sayed and L. D. Partain, "Reliability of low-cost CdS/Cu₂S solar cells," in *Electronics Letters*, vol. 10, no. 9, pp. 163-164, 2 May 1974.

VITA

Benjamin Reed Wells was born in Lexington, Kentucky. He received his Bachelor of Science degree in Electrical Engineering from the University of Kentucky in 2015. He has worked as a research assistant in the Electronic Devices Research Laboratory (EDRL) from 2018-2020 and as a teaching assistant from 2019-2020 at the University of Kentucky.